# Impact of Spectral Aerosol Radiative Forcing at the Izaña Observatory during the August 2023 Extreme Wildfires.

Rosa D. García[1,2,3], África Barreto[2,3], Victoria E. Cachorro[3], Pablo González-Sicilia[1,2,3], Sergio Léon-Luis[1,2,*], Ayoze Álvarez-Hernández[1,2], Juan José Bustos[2], Ramón Ramos[2], Fernando Almansa[4,2], Óscar Álvarez-Losada[1,2], Yenny González[4,2], Pedro Pablo Rivas[2], and Carlos Torres[2]

[1]TRAGSATEC, 28037, Madrid, Spain
[2]Izaña Atmospheric Research Center (IARC), State Meteorological Agency of Spain (AEMET), 38108, Santa Cruz de Tenerife, Spain
[3]Atmospheric Optics Group of Valladolid University (GOA–UVA), Valladolid University, Valladolid, Spain
[*]Now: Department of Physics, La Laguna University, San Cristóbal de La Laguna, 38206, Spain
[4]Scientific department, CIMEL Electronique, Paris, 75011, France

**Correspondence:** África Barreto (abarretov@aemet.es)

**Abstract.** Extreme wildfires represent a highly variable source of atmospheric aerosols with potentially strong impacts on surface solar radiation. In August 2023, an exceptional wildfire on Tenerife (Canary Islands, Spain) reached the neighbourhoods of the Izaña Observatory (IZO, 2400 m a.s.l.). This near-source configuration enabled a rare observational characterisation of the spectral radiative effects of biomass-burning aerosols. During the most intense phases of the event (17–18 August), aerosol optical depth (AOD) at 500 nm reached extreme values of 3.63 and 2.25, respectively, with Ångström Exponent (AE) above 2, indicating a strong dominance of fine-mode smoke particles. Spectral measurements of global-horizontal, direct-normal and diffuse-horizontal solar irradiance (300–1100 nm) show a pronounced attenuation of direct and global irradiances, particularly in the visible range, together with a strong enhancement of diffuse radiation. Relative to clean-sky conditions, daily global irradiance decreased by 21–27 %, while direct-normal irradiance was reduced by 72–99 %. Spectral aerosol radiative forcing and radiative forcing efficiency at the surface were quantified using radiative transfer simulations under pristine atmospheric conditions as a reference. The integrated spectral radiative forcing (300-1100 nm) for global irradiance reached -395 and -299 W $m^{-2}$ on 17 and 18 August, respectively, indicating strong surface cooling dominated by scattering processes. Maximum forcing and efficiency occurred in the visible spectral range, consistent with the optical properties of freshly emitted smoke aerosols. At the same time, increases in the amount of present particles, equivalent black carbon (eBC) and greenhouse gases ($CO_2$, $CH_4$ and CO) confirm the direct influence of the wildfire plume on atmospheric composition at IZO. These observations provide one of the few detailed spectral assessments of surface radiative forcing by extreme biomass-burning aerosols at a high-altitude site and highlight the need to accurately represent fine-mode smoke aerosols in radiative transfer and climate models.

## 1 Introduction

Wildfires are increasingly recognised as key agents of changes on the atmosphere, influencing air quality, the planetary radiation budget, and the climate system. According to the IPCC Sixth Assessment Report (IPCC, 2023), the total anthropogenic effective radiative forcing in 2019 relative to preindustrial conditions is estimated at 2.72 [1.96–3.48] W $m^{-2}$ (medium confidence) (Forster et al., 2021). This positive forcing arises mainly from the continuous accumulation of greenhouse gases (GHGs), partially offset by the cooling effect due to anthropogenic aerosols. IPCC (2023) also reports a $\sim$0.43 W $m^{-2}$ ($\sim$19 %) increase in the total radiative forcing since the Fifth Assessment Report (IPCC, 2013). Most of this increment, around 0.34 W $m^{-2}$, is attributed to additional GHG emissions since 2011, while the remaining increase, around 0.09 W $m^{-2}$, reflects improved estimates of aerosol contributions, owing to enhanced observational datasets and progress in representing aerosol–radiation and aerosol–cloud interactions in climate models.

Among the different aerosol sources, biomass burning stands out as one of the most variable and least predictable in terms of emissions and radiative effects. Aerosols produced by wildfires encompass a heterogeneous mixture of absorbing components (e.g., black carbon, brown carbon) and scattering species (organic and inorganic matter). Their radiative influence depends strongly on their optical and microphysical characteristics, vertical distribution within the atmosphere, and interactions with clouds and underlying surfaces. These complexities generate significant uncertainty when assessing the radiative forcing associated with wildfire emissions.

In recent decades, wildfire activity has intensified across many regions of the globe, a trend strongly linked to rising global temperatures, a higher frequency of extreme heat events, and widespread transformations in land use and droughts (Cunningham et al., 2024; Elmqvist et al., 2025; WMO, 2023). Current estimates indicate that wildfires burn 3.5–4.6 million $km^2$ each year, equivalent to about 2–3 % of Earth's land surface (Guo et al., 2025). Beyond their ecological impacts, these events represent a major atmospheric source of trace gases and aerosols, with significant implications for air quality and climate. Areas with Mediterranean-type climates—such as southern Europe, California, central Chile, southwestern Australia, and parts of South Africa—are particularly prone to suffer large and intense fires due to their hot and dry summers, and strong interannual climatic variability. Within Europe, Mediterranean countries account for nearly 85 % of the total burned area (Sicard et al., 2012; Amatulli et al., 2013; Zhuravleva et al., 2017; San-Miguel-Ayanz et al., 2023). Recent high-impact fire seasons, including the 2016 Madeira fires (Navarro et al., 2017) and the 2023 wildfire crisis in Greece (Masoom et al., 2023; Michailidis et al., 2024; Koukouli et al., 2025), have highlighted the growing societal exposure to fire hazards, often resulting in mass evacuations, severe damage to infrastructures, and major economic losses (Jones et al., 2024; Elmqvist et al., 2025). At the same time, shifts in atmospheric circulation—particularly the increased frequency and intensity of extreme heatwaves and droughts—together with the desiccation of continental air masses, such as Saharan advection episodes, create highly favourable conditions for fire ignition and rapid fire spread. This is the case for one of the most frequent types of heatwaves over Europe, which often occur in the presence of intrusions of desert dust particles originating from North Africa (WMO, 2023). The Canary Islands (Spain) are regularly influenced by such Saharan intrusions, which constitute a prominent and recurrent component of the regional

atmospheric dynamics (Cuevas et al., 2017; Barreto et al., 2022). These air masses are typically characterised by exceptionally low humidity and temperatures well above climatological values (Correa and Dorta, 2025).

In August 2023, a large-scale wildfire on Tenerife (Canary Islands) allowed researchers to investigate, as an exceptional natural experiment, the atmospheric impacts of intense biomass burning. It was the second largest wildfire on Tenerife and the third in the Canary Islands since systematic monitoring began in 1983 (Correa and Dorta, 2025). The fire burned more than 13.000 hectares across 12 municipalities and advanced, reaching the close vicinity of the Izaña Observatory (IZO), a high-mountain research station operated by the Spanish State Meteorological Agency (AEMET) through the Izaña Atmospheric Research Center (IARC). Although the observatory infrastructure was not damaged, the extreme closeness of the fire enabled direct observations of its impact in the low free troposphere. This unusual scenario provided a unique opportunity to examine how intense wildfire emissions affect a wide range of atmospheric parameters routinely measured at IZO. As part of the World Meteorological Organization (WMO) Global Atmosphere Watch (GAW) programme, and of the European Research Infrastructure Consortia ACTRIS (Aerosols, Clouds and Trace Gases Research Infrastructure) and ICOS (Integrated Carbon Observation System), IZO maintains long-term records of greenhouse gases, aerosols, solar radiation, and reactive gases, among other variables (Laj et al., 2024; Cuevas et al., 2023, 2024). During the wildfire episode, pronounced anomalies were detected across these datasets, offering valuable insights into the radiative and compositional impacts of smoke intrusions at this remote high-elevated site.

This study aims to characterise the spectral aerosol radiative forcing and efficiency exerted by wildfire aerosols. Such spectral studies are very scarce, and most existing works focus on the impact of wildfires on irradiance without considering their effects on radiative forcing or efficiency. The extreme 2023 fire episode occurred only a ~~few metres from~~ ≈ 280 m north and 620 m east of the spectroradiometer operating at IZO, providing a unique opportunity to directly observe the spectral radiative signal of fresh smoke under near-source conditions.

The measurements used in this study were conducted within the framework of the WMO Measurement Lead Centre (MLC) for Aerosols and Water Vapour Remote Sensing Instruments. The structure of the paper is as follows: Section 2 presents the main features of the Izaña Observatory and the instrumentation used in this work. Section 3 describes the methodology applied to quantify aerosol spectral radiative forcing and radiative efficiency. Section 4 provides an overview of the wildfire event and presents the key results. Finally, Section 5 summarises the main conclusions of the study.

## 2 Site description and instruments

### 2.1 Site description

The datasets analysed in this study were obtained at the Izaña Observatory (IZO), operated by the Izaña Atmospheric Research Center (IARC) of the Spanish State Meteorological Agency (AEMET) (http://izana.aemet.es, last access on 15 April 2025). IZO is located on the island of Tenerife (Canary Islands, Spain (28.3° N, 16.5° W)), at an altitude of 2400 m a.s.l. (Figure 1a), and is typically situated above a quasi-permanent temperature inversion layer. This persistent atmospheric feature limits the vertical transport of locally generated pollutants from lower altitudes, ensuring that the measurements collected at the site are

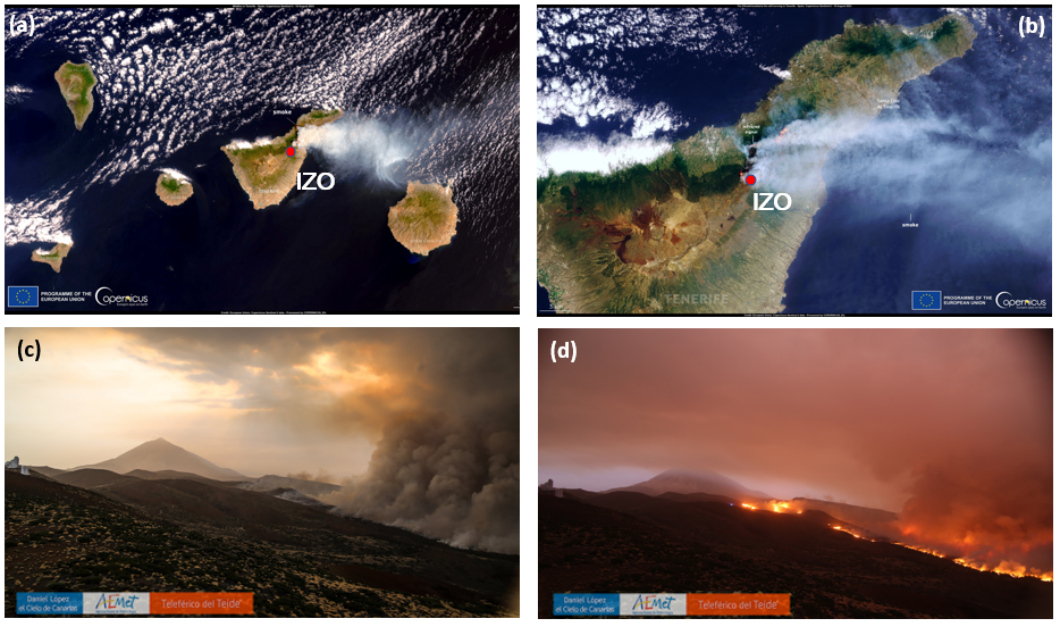


**Figure 1.** (a,b) Copernicus Sentinel-2 image acquired on 18 August over Tenerife. The red dot marks the location of the Izaña Observatory (Canary Islands, Spain). (c,d) Images of Teide National Park captured on 17 and 18 August 2023 from Izaña Observatory (Teide Cloud Laboratory Project, project from Izaña Observatory by Daniel López).

mostly representative of free-tropospheric conditions (Cuevas et al., 2013). Consequently, IZO offers an exceptional environment for both in situ and remote sensing observations of trace gases and aerosols. The combination of a stable total ozone column, extremely low water vapour content, reduced aerosol loading, and the frequent occurrence of clean, cloud-free skies makes the observatory an ideal reference site for calibration and validation activities (more details in Cuevas et al. (2024)).

## 2.2 Instruments

### 2.2.1 EKO RSB spectroradiometer

In this study, global ($GHI_\lambda$), direct-normal ($DNI_\lambda$), and diffuse ($DHI_\lambda$) spectral irradiance were measured using an EKO MS-711 spectroradiometer equipped with a rotating shadow band (hereafter EKO RSB; Figure 2a). The instrument operates over the 300–1100 nm range, with a spectral step of approximately 0.4 nm and a nominal full width at half maximum (FWHM) of less than 7 nm. It acquires one spectrum per minute, with exposure times automatically adjusted between 10 ms and 5 s according to irradiance levels and sky conditions. Each measurement cycle consists of four sequential acquisitions at different shadow band positions (Figure 2b), completed in less than one minute (Pó et al., 2018; Takamura and Khatri, 2021). Thus, at the $1^{st}$ position the shadow band rests outside the instrument's field of view (FOV); at the $2^{nd}$ position the shadow band stops at -5° from the solar disk; at the $3^{rd}$ position the EKO RSB covers the solar disk to perform the diffuse measurement and

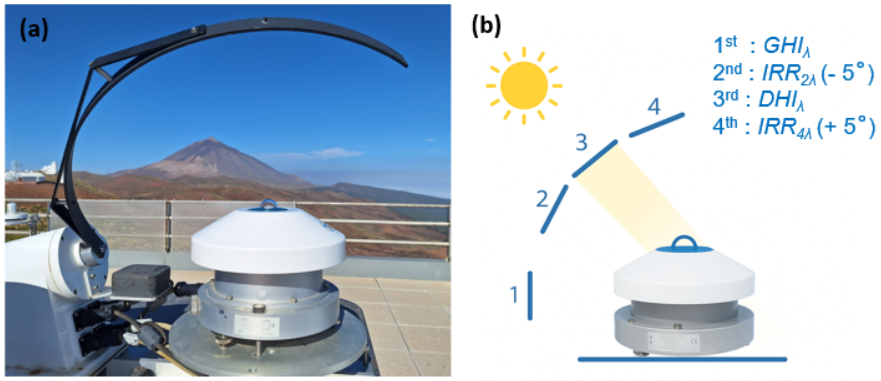


**Figure 2.** (a) The EKO RSB grating spectroradiometer installed at Izaña station. (b) EKO RSB band sweeping positions (Figure adapted from Pó et al. (2018))

.

finally at the $4^{th}$ position the shadow band stops at +5° ~~after~~ beyond the solar disk. The spectral $GHI_\lambda$ and $DHI_\lambda$ irradiances are measured in the $1^{st}$ and $3^{rd}$ positions, respectively. From these two measurements, the $DNI_\lambda$ spectral irradiance is derived as follows:

$$DNI_\lambda = \frac{(GHI_\lambda - DHI_\lambda)}{cos(SZA)} \tag{1}$$

where SZA is the solar zenith angle. The $2^{nd}$ ($IRR_{2\lambda}$) and $4^{th}$ ($IRR_{4\lambda}$) positions are used to estimate the amount of diffuse irradiance lost due to the EKO RSB's partial obstruction of the sky, and a correction is applied to $DHI_\lambda$ as follows:

$$DHI_{\lambda corr} = DHI_\lambda + (GHI_\lambda - \frac{IRR_{2\lambda} + IRR_{4\lambda}}{2}) \tag{2}$$

### 2.3 Ancillary instruments

#### 2.3.1 AERONET Cimel Sun Photometer

The aerosol columnar optical properties (aerosol optical depth (AOD), Ångström Exponent (AE), and fine/coarse AOD) used in this study were obtained from measurements performed with a Cimel CE318-T sun–sky–lunar photometer, the reference instrument of the AErosol RObotic NETwork (AERONET), a global federated network established in 1993 for the long-term monitoring and characterization of atmospheric aerosols (Holben et al., 1998; O'Neill et al., 2003; Barreto et al., 2016; Giles et al., 2019; O'Neill et al., 2023). This instrument is an automatic scanning filter radiometer operating at nine nominal wavelengths (340, 380, 440, 500, 675, 870, 937, 1020, and 1640 nm), with a FOV of 1.3° (Holben et al., 1998; Torres et al.,

2013) and a FWHM of 10 nm, except for 340, 380, and 1640 nm, which have bandwidths of 2, 4, and 25 nm, respectively. Izaña Observatory is an AERONET calibration site for reference instruments (Toledano et al., 2018).

In this study, Level 2.0 AERONET direct-sun products (AOD, AE, and fine/coarse AOD) were used to retrieve aerosol properties for 17 August. However, for 18 August, Level 1.0 AOD data were employed because the extreme intensity of the event caused most photometric measurements to be misclassified as cloudy by the AERONET quality-control algorithms, as previously reported for the February 2020 desert dust outbreak (Cuevas et al., 2021). To ensure retrievals under clear-sky conditions, only measurements identified as clear sky by the procedure of Long and Ackerman (2000), as adapted for Izaña by García et al. (2014), were considered. Furthermore, inversion products (such as single scattering albedo and asymmetry parameter) were not used because the available data were insufficient for this study.

#### 2.3.2 Micro-Pulse Lidar

Relative attenuated backscatter profiles and volume depolarization ratios were measured with a Micro-Pulse Lidar (MPL, model MPL-4B) operating at IZO during the forest fire outbreak at the station. This type of lidar is an eye-safe elastic lidar operating continuously (24/7) at 532 nm with a low-pulse energy laser (5–6 $\mu$J) and a repetition rate of 2.5 kHz (Welton et al., 2001; Campbell et al., 2002). The MPL-4B version features depolarization capability, which is useful for identifying depolarizing particles (Flynn et al., 2007). As the reference instrument of the National Aeronautics and Space Administration Micro-Pulse Lidar Network (NASA-MPLNet), signal processing and retrieval products are centralised at the network level (Welton et al., 2018). According to Campbell et al. (2002) and Welton et al. (2018), this processing includes corrections for detector deadtime and dark current, laser–detector after-pulse, overlap, and polarization calibrations. MPLNet Version 3, Level 1.5 aerosol products were used in this study.

#### 2.3.3 TEOM

~~Bulk~~ Surface measurements of bulk mass concentrations were measured using the TEOM 1405-DF instrument (Thermo Fisher Scientific$^{TM}$). This instrument operates by collecting particles onto a vibrating substrate maintained at constant amplitude. As particles accumulate on the filter, the increasing mass causes a decrease in the vibration frequency. The total particle concentration (PM, Particulate Matter) is then calculated from this frequency change as a function of aerosol mass accumulation over time (Patashnick et al., 1983).

The TEOM 1405-DF measures the coarse PM and $PM_{2.5}$ fractions of $PM_{10}$, which are separated by a virtual impactor and collected on two dedicated filters. $PM_{10}$ concentration is obtained by summing the $PM_{2.5}$ and coarse PM fractions. The instrument has a resolution of approximately $\pm 5$ $\mu$g m$^{-3}$ for 10-minute sampling intervals (Rodríguez et al., 2012).

#### 2.3.4 ~~MAPP~~MAAP

Surface Equivalent Black Carbon (eBC) mass concentrations were obtained from two Multi-Angle Absorption Photometer instruments (MAAP; Thermo$^{TM}$) with separated sampling lines for $PM_{10}$ and $PM_1$ using virtual impactors. MAAP instruments

measure the change in transmittance of a 637 nm light source through a filter tape as particles are deposited. Additionally, the instrument measures backscattered light from the sample and filters using two detectors positioned at different angles. This configuration enables determination of the absorption of the aerosol sample through a radiative transfer scheme with a relative uncertainty of $\pm 12\%$ (Petzold and Schönlinner, 2004). The measured absorption is then converted to eBC mass concentration using a mass absorption cross-section of 6.6 $m^2$ $g^{-1}$, defined in the instrument firmware following ACTRIS guidelines (Müller et al., 2011; Petzold et al., 2013).

### 2.3.5 Integrating Nephelometer

~~Total~~ Surface total scattering coefficient data ($\sigma_{scat}$ ($\lambda$)) were collected with a TSI$^{TM}$ integrating nephelometer (model 3563) at three wavelengths (450, 550, and 700 nm). From that, the Scattering Ångström Exponent (SAE; Ångström (1930)) was calculated using the 450 ($\lambda_1$) nm and 700 ($\lambda_2$) nm total scattering values according to the following relation:

$$SAE = -\frac{ln(\sigma_{scat}(\lambda_1)/\sigma_{scat}(\lambda_2))}{ln(\lambda_1/\lambda_2)} \tag{3}$$

The instrument is calibrated annually using $CO_2$ as the high span gas and filtered air as the low span gas. The averaging time is set to 1 minute, and the instrument performs routine 5-minute zero checks every hour. Additional corrections for truncation and non-Lambertian illumination were applied to the data following the method described by Anderson and Ogren (1998), which gives a reported uncertainty of approximately 7 $\%$ for scattering values (Heintzenberg et al., 2006). Sampling is performed through an inlet assembly with a $PM_{10}$ virtual impactor.

The Single Scattering Albedo (SSA; $\omega_0$) was calculated following Valenzuela et al. (2015), by combining the total scattering coefficient ($\sigma_{scat}(\lambda)$) from the nephelometer and the absorption coefficient ($\sigma_{abs}(\lambda)$) derived from the MAAP measurements. The absorption coefficient was obtained by multiplying the eBC mass concentration by the mass absorption cross-section of 6.6 $m^2$ $g^{-1}$, with a correction factor of 1.05 applied to account for the shift in the MAAP light source wavelength (Müller et al., 2011). SSA was then computed at 637 nm using:

$$\omega_0(\lambda) = \frac{\sigma_{scat}(\lambda)}{\sigma_{scat}(\lambda) + \sigma_{abs}(\lambda)} \tag{4}$$

where $\sigma_{scat}$ ($\lambda$) was interpolated to 637 nm from the nephelometer measurements using the SAE, in order to match the MAAP absorption wavelength.

All in situ aerosol measurements were conducted in the same laboratory, under controlled environmental conditions, with ambient temperature maintained at 21 $\pm$ 2 °C. Data points were subsequently filtered to exclude measurements recorded at relative humidity above 40 $\%$ to ensure dry sampling conditions.

### 2.3.6 Picarro Cavity Ring-Down Spectrometer

Dry-air mole fractions of $CO_2$, $CH_4$, and CO were measured using a Picarro G2401 analyser based on cavity ring-down spectroscopy (Crosson, 2008). The analyser operates continuously at IZO under the WMO-GAW programme (Cuevas et al., 2024) and is calibrated monthly using four multi-species tertiary standards prepared by the WMO Central Calibration Laboratory (https://gml.noaa.gov/ccl/, last access on 25 November 2025). Measurements are reported on the following WMO scales: X2019 for $CO_2$, X2004A for $CH_4$ and X2014A for CO. The system provides high-precision measurements with typical $1\sigma$ uncertainties for 1-minute averages of 0.013 ppm ($CO_2$), 0.19 ppb ($CH_4$), and 0.87 ppb (CO) when analysing calibration tanks (Gómez-Pelaez et al., 2019).

Ambient air is sampled from the roof of the IZO building and passed through a cold trap at -70 °C to remove water vapour and ensure dry-air conditions. The instrument acquires data every 2 seconds, but in this study we used 1-minute averaged values. Further details on the calibration procedure and instrument characterisation can be found in Gómez-Pelaez et al. (2019).

## 3 Methodology: Spectral radiative forcing and efficiency

To quantify changes in the energy budget of the Earth–atmosphere system, the concept of radiative forcing ($\Delta$F) is introduced as an indicator of these changes (IPCC, 2023). In this study, we focus on the aerosol effect, particularly that associated with biomass burning. The radiative forcing ($\Delta$F) is defined as follows, considering its dependence on wavelength and solar zenith angle:

$$\Delta F^{\text{eff}}(\lambda, SZA) = \frac{\Delta F(\lambda, SZA)}{\text{AOD}(\lambda, SZA)} \tag{5}$$

In this equation, $F\downarrow^{A}$ represents the downward irradiance at the surface in the presence of atmospheric aerosols, while $F\downarrow^{C}$ corresponds to the irradiance expected under clean or pristine atmospheric conditions, obtained from radiative transfer simulations. Under this sign convention, negative values of $\Delta$F($\lambda$,SZA) indicate a cooling influence of aerosols at the surface, whereas positive values denote a warming effect.

After computing $\Delta$F($\lambda$,SZA), the spectral aerosol radiative forcing efficiency, $\Delta F^{eff}$($\lambda$,SZA), can be defined as:

$$\Delta F^{\text{eff}}(\lambda, SZA) = \frac{\Delta F(\lambda, SZA)}{\text{AOD}(\lambda, SZA)} \tag{6}$$

where AOD($\lambda$,SZA) represents the aerosol optical depth at the specified wavelength and solar zenith angle, which in this case was obtained from direct-normal spectral irradiance measurements ($DNI_\lambda$) recorded by the EKO RSB following the methodology described in García et al. (2020).

To estimate $F^{\downarrow C}$($\lambda$,SZA), the libRadtran radiative transfer model was used (Mayer and Kylling, 2005; Emde et al., 2016). This model has been extensively tested at the Izaña Observatory (e.g. García et al. (2014); García et al. (2019); García et al. (2020)). The radiative transfer equation (RTE) solver employed was the DIScrete Ordinates Radiative Transfer (DISORT)

algorithm (Stamnes et al., 1988), which is based on a multi-stream discrete ordinates method using 16 streams. Corrections for Earth's sphericity were applied for SZA greater than 70° (Dahlbäck and Stammes, 1991). For each simulation, the $GHI_\lambda$, $DNI_\lambda$ and $DHI_\lambda$ spectral irradiances were computed in the 300–1100 nm range with a 1 nm spectral step (García et al., 2023; Cachorro et al., 2025).

The forcing ($\Delta$DF) and radiative forcing efficiency ($\Delta DF^{eff}$) in different spectral ranges have been determined from the following equation:

$$\Delta DF = \int_{\lambda_1}^{\lambda_2} \Delta F(\lambda, SZA) \cdot d\lambda \tag{7}$$

## 4 Results

### 4.1 Description of the event

In August 2023, an extensive wildfire on the island of Tenerife provided a unique natural laboratory for investigating the atmospheric effects of biomass-burning aerosols. Although IZO remained physically unaffected by the fire, its proximity to the burning area offered an exceptional opportunity to monitor the resulting smoke plume and examine its evolution under free-tropospheric conditions. This situation enabled the direct characterisation of the optical, microphysical and radiative properties of wildfire-derived aerosols, thus yielding valuable insight into their short-term influence on the regional radiation budget and atmospheric composition.

Climatic conditions in the Canary Islands during August 2023 created a highly favourable environment for wildfire development. According to AEMET (AEMET, 2024), this month was exceptionally dry, with a mean temperature of 25.4 °C and a positive anomaly of +2.3 °C compared to the 1991–2020 reference period, ranking as the warmest August since 1961. A heatwave between 10 and 14 August (AEMET, 2023) pushed temperatures close to 40 °C, while relative humidity fell below 20 % and wind gusts exceeded 30 km $h^{-1}$ in Tenerife, as recorded at the AEMET station in Candelaria (463 m a.s.l.), near to the origin point of the subsequent wildfire. Although the fire ignited one day after the maximum alert had been lifted-coinciding with notably milder conditions (27.3 °C maximum temperature; 75 % minimum humidity, Correa et al. (2025)), the severe desiccation of the forest fuel over prior weeks was decisive in enabling its rapid spread. Supporting this, the base of the subsidence-induced thermal inversion remained below 600 m a.s.l. from 11 to 19 August, maintaining a warm and dry free troposphere above the island (Correa and Dorta, 2025; Correa et al., 2025).

During the period 15–31 August 2023, a pronounced aerosol episode was detected at IZO on 17 and 18 August (Figure 1 c, d and Figure 3). The AOD values increased sharply across all measured wavelengths (340–870 nm), reaching maxima of 4.81 and 3.63 at 340 and 500 nm, respectively, on 17 August, and 4.10 and 2.25 at 340 and 500 nm, respectively, on 18 August. Simultaneously, AE>2 on both days (2.06 on 17 August and 2.04 on 18 August) (see Table 1), indicating a predominance of fine-mode particles. These features are characteristic of biomass-burning aerosol intrusions and are comparable to those

**Table 1.** Aerosol optical and microphysical properties corresponding to the maximum of $AOD_{500nm}$ values performed at IZO on 17 and 18 August 2023. Parameters included are: AOD (500 nm), AE (440–870 nm), Total (500 nm), Fine (500 nm), and Coarse-mode (500 nm), fine-mode fraction (FMF, 500 nm), mass concentration of $PM_{10}$ ($\mu g\ m^{-3}$) , ratio between $PM_{2.5}$ and $PM_{10}$, and the SAE (450–700 nm)

| Case | SZA (°) | AOD | AE | Total | Fine | Coarse | FMF | $PM_{10}$ | $PM_{2.5}/PM_{10}$ | SAE |
|---|---|---|---|---|---|---|---|---|---|---|
| 17-08-2023 11:56 | 22.7 | 3.63 | 1.71 | 3.61 | 3.58 | 0.03 | 0.99 | 393.17 | 0.81 | 1.78 |
| 18-08-2023 15:46 | 39.1 | 2.25 | 2.04 | 2.24 | 2.12 | 0.13 | 0.94 | 91.66 | 0.66 | 2.14 |

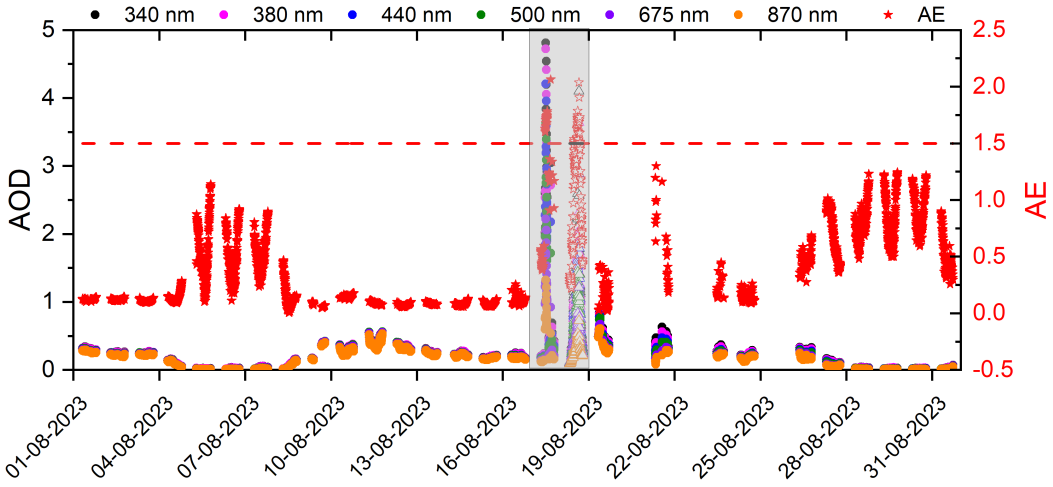


**Figure 3.** Time series of AOD at different wavelengths (left axis: 340 nm, black dots; 380 nm, magenta dots; 440 nm, blue dots; 500 nm, green dots; 675 nm, violet dots; and 870 nm, orange dots) and AE (440–870 nm) (right axis, red stars) during August 2023 at IZO. The red dashed lines and green area indicate the thresholds defined for biomass-burning conditions (AE > 1.5). The data are from the AERONET network, filled symbols correspond to Version 2.0 data, while open symbols represent Version 1.0 data.

reported by Masoom et al. (2023) during the extreme wildfire episode in Greece in August 2021, where AOD values up to 3.6 at 500 nm~~and~~ , AE up to 2.4 (440–870 nm), and fine-mode fractio (FMF) values around 0.98 were observed. Therefore, the following study focuses on the events recorded on 17 and 18 August.

A more detailed characterisation of the aerosol optical and microphysical properties during this episode is presented in Figure 4. Spectral AOD and AE evolution is presented in Figure 4a. The AOD decomposition at 500 nm during the event (Figure 4b) shows that the fine-mode component dominated the total column, with the ~~fine-mode fraction (FMF )~~ FMF approaching unity. On 17 August, the high AE and FMF values (∼1.5 and >0.8, respectively) indicate a fine-mode–dominated aerosol population, typical of freshly emitted smoke. As the event evolved (18–19 August), AE decreased below 0.8 and FMF below 0.4, revealing aerosol mixing with coarse dust particles within the plume. Figure 4c confirms this dominance, with data points from 17 and 18 August clustering in the region of high AE (> 1.5) and high FMF (> 0.8) (Figure 4c), indicative of fine-mode aerosols from biomass burning (Eck et al., 2001; O'Neill et al., 2023). These values are similar to those reported

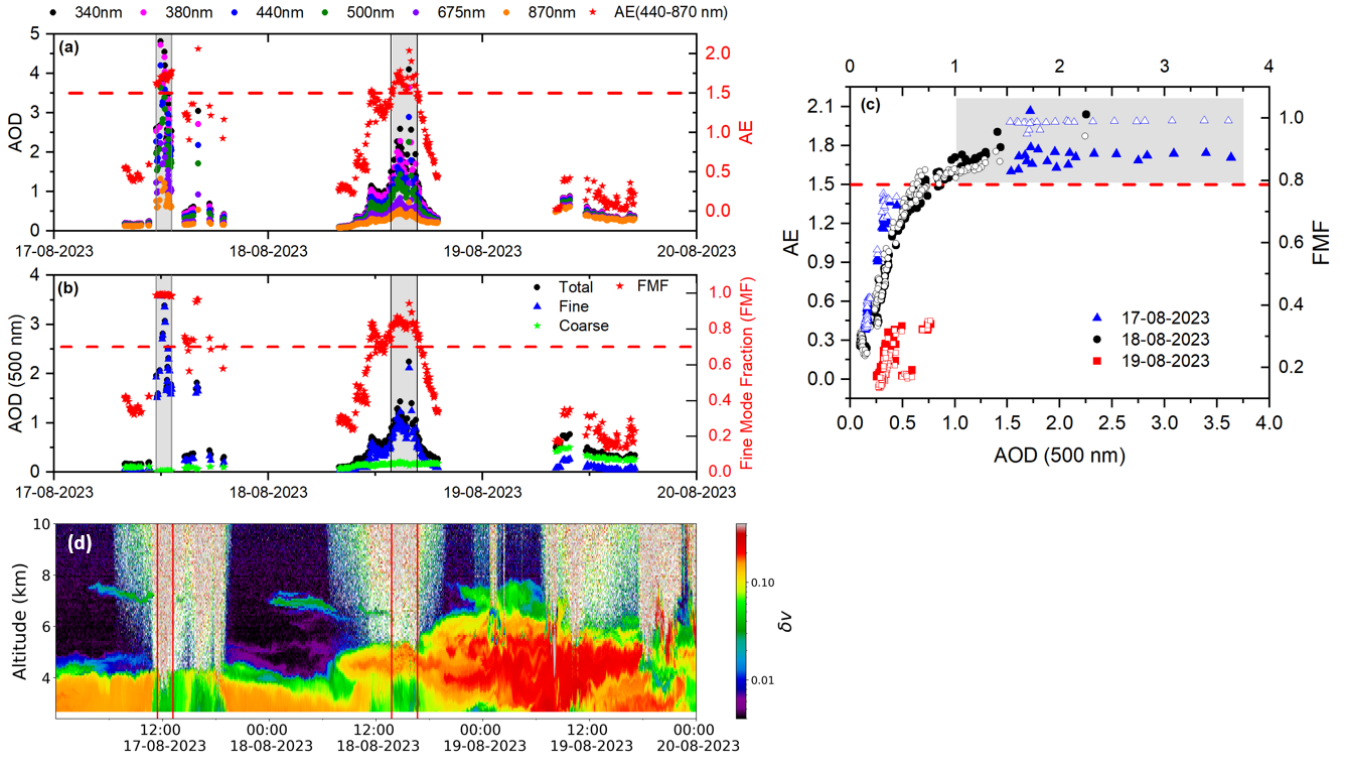


**Figure 4.** Time series of (a) AOD at different wavelengths (left axis: 340 nm, black dots; 380 nm, magenta dots; 440 nm, blue dots; 500 nm, green dots; 675 nm, violet dots; and 870 nm, orange dots) and AE (440–870 nm) (right axis, red stars); (b) total (black dots), fine-mode (blue triangles), and coarse-mode (green stars) AOD at 500 nm (left axis), together with FMF (right axis, red stars). Grey shaded areas highlight the two most notable fire events. (c) Scatterplot of AE versus AOD at 500 nm (filled symbols) and FMF versus AOD at 500 nm (open symbols) between 17 and 19 August 2023. The grey shaded area marks the thresholds defined for biomass-burning conditions (AE > 1.5 and $AOD_{500nm}$ > 1.0). The data are from the AERONET network, Version 3, Level 1.5 for 17 and 19 August, and Level 1.0 for 18 August. (d) Temporal evolution of Volume Depolarization Ratio ($\delta$v) measured between 17 and 19 August with MPL-4B Lidar at IZO.

by ~~Masoom et al. (2023)~~ Masoom et al. (2023); Michailidis et al. (2024) for the extreme wildfires that occurred in Greece in August ~~2021.~~ 2021 and 2023, respectively, as well as to those reported by Filonchyk and Peterson (2024) at the El Arenosillo site in southern Europe as a result of the 2023 Canadian forest fires.

The vertical distribution of aerosols derived from lidar observations (Figure 4d) reveals that the fresh smoke layer extended up to 4 km a.s.l. on 17 and 18 August, with enhanced backscatter coefficients (not shown) and low volume depolarization ratios ($\delta$v) of 0.05–0.10 during the most intense fire periods (grey areas in Figure 4). For the 17 August event (no product available for 18 August), $\delta$p values ranged from 0.05 to 0.12. These values are consistent with those reported by Nepomuceno Pereira et al. (2014); Haarig et al. (2018) for fresh smoke, who found $\delta$p values around 0.05. According to these authors, such low $\delta$p

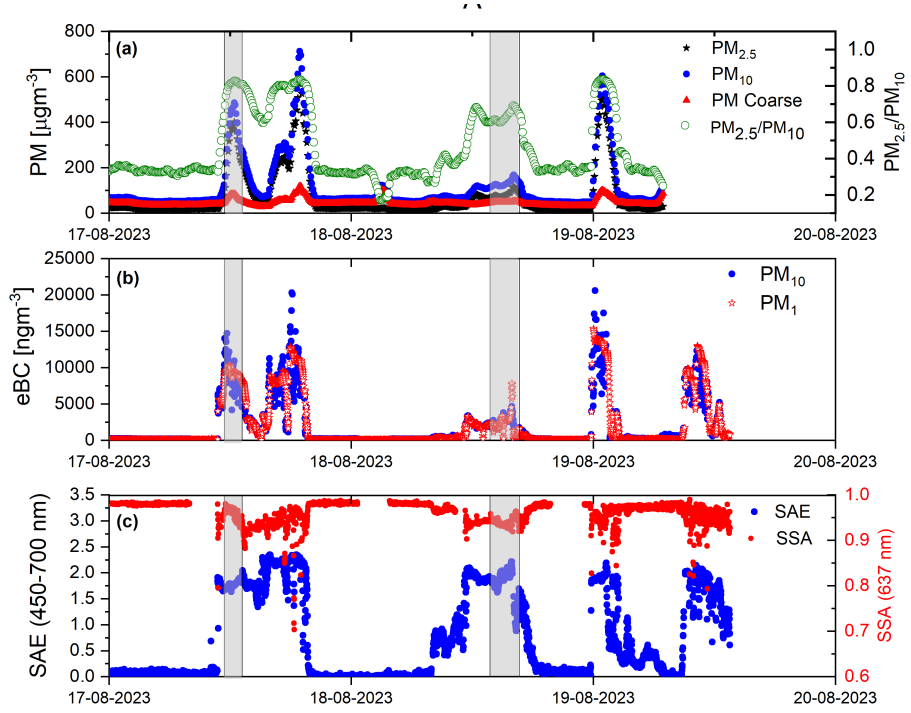


**Figure 5.** Time series of in situ aerosol measurements at IZO from 17 to 20 August 2023. (a) Mass concentrations of $PM_{10}$ (black stars), $PM_{2.5}$(blue circles), ~~and~~ coarse-mode PM (red triangles) and $PM_{2.5}/PM_{10}$ ratio (green dots, right axis). (b) Equivalent Black Carbon (eBC) concentrations for $PM_{10}$ (blue circles) and $PM_1$ (red stars) ~~and~~ (c) SAE (450–700 nm; blue circles) and ~~$PM_{2.5}/PM_{10}$ ratio~~ SSA (at 637 nm; red ~~dots~~circles, right axis). Shaded areas indicate the periods corresponding to the maximum AOD values observed on 17 and 18 August.

values indicate the dominant presence of spherical particles, mainly composed of a solid soot core coated with a liquid sulfate shell (Haarig et al., 2018).

An elevated layer reaching 7–8 km a.s.l. appeared on 19 August, characterised by high $\delta$v and $\delta$p values (up to 0.34 and 0.36, respectively), corresponding to the Saharan dust plume transported to IZO. The influence of coarse mineral dust particles is also consistent with the low AE values observed in Figures 4a, 4b, and 4c. After 19 August, both AOD and backscatter intensity decreased rapidly, marking the end of the episode. These results agree with those reported by González et al. (2025), who found similar values for both fresh aerosols from the same fire event and for mineral dust measured at Izaña using a dual-wavelength depolarisation elastic lidar (Cimel CE376). This elevated layer reached the altitude of Izaña between 05:00 and 09:00 UTC on 19 August and again after 12:00 UTC on the same day.

~~During this local event ,~~ This local event was also characterised using in situ surface measurements, complementing remote-sensing observations. $PM_{10}$ and $PM_{2.5}$ concentrations experienced a substantial increase compared to their typical levels. In particular, $PM_{10}$ and $PM_{2.5}$ (Figure 5a) reached peak concentrations of 712.19 and 594.64 $\mu$g m$^{-3}$, respectively, representing an increase of approximately 700 $\mu$g m$^{-3}$ above typical values for the station (Rodríguez et al., 2011).

Five significant peaks were identified in the time series (Figure 5), with one peak excluded from TEOM data (Figure 5a) due to relative humidity filtering (Section 2.3). These peaks occurred on three consecutive days: two on 17 August (late morning and afternoon), one on 18 August afternoon, and two on 19 August, one at midnight and the other encompassing from the morning to midday. The peaks on 17 August morning and 18 August afternoon (shaded areas in Figure 5) coincided with fire events identified from columnar properties (Figure 4). The elevated $PM_{10}$ and $PM_{2.5}$ concentrations ~~during these events~~ within these periods indicate direct impacts from wildfire smoke plumes at the observatory, reaching maximum values of 485.19 and 167.80 $\mu$g m$^{-3}$ for $PM_{10}$ and 401.53 and 116.26 $\mu$g m$^{-3}$ for $PM_{2.5}$ (17 and 18 August). The eBC concentrations reached record values for the station (González et al., 2025) with peaks of 14.74 and 10.31 $\mu$g m$^{-3}$ for the $PM_{10}$ and $PM_1$ size cuts on 17 August, and 4.69 and 7.81 $\mu$g m$^{-3}$ on 18 August. ~~The SAEand~~ Correspondingly, the SAE, $PM_{2.5}/PM_{10}$ ratio~~provided~~ , and SSA, which provide complementary information on aerosol size ~~distribution, with SAE values of 2.34 and 2.21, and $PM_{2.5}/PM_{10}$ ratios of~~ and optical properties, reached maximum values of 1.93, 0.83~~and 0.69 for~~ , and 0.98 on 17 ~~and~~ August, and 2.21, 0.69, and 0.96 on 18 August, respectively. These values collectively confirm the dominance of fine, light-scattering wildfire-originated particles during the selected events.

The temporal evolution of ~~the event~~ ground-level measurements from 17 to 20 August (Figure 5), revealed the successive entrance and exit of smoke-dominated air masses. Their progressive mixing with desert dust was reflected by oscillations in the $PM_{2.5}/PM_{10}$ ratio from $\sim$0.8 to $\sim$0.3, accompanied by a decrease in the SAE from values above 2 to below 0.2. This behaviour was also evident in columnar-integrated measurements on 17 and 18 August. In contrast, the comparison between column-integrated and in situ measurements on 19 August revealed several complications. First, the midnight event could not be measured in the atmospheric column due to the limited availability of lunar photometry data, which is only available between the first and last quarters of the lunar cycle (Barreto et al., 2016). Second, it is important to emphasise that the detection of short-lived aerosol events may differ between in situ and remote-sensing (column-integrated) techniques because each method samples different atmospheric layers, and local conditions at the station level may not be representative of the column-averaged aerosol load. This discrepancy was evident on 19 August, where the morning event showed fine particles at the surface level, with eBC concentrations peaking at 12.33 and 13.00 $\mu$g m$^{-3}$ in $PM_{10}$ and $PM_1$ fractions, and SAE reaching 2.19 (Figures 5b and 5c), contrasting with the columnar measurements of FMF and AE (Figures 4a and 4b), which indicated coarser particles with values below 0.4 and 0.5, respectively. The lidar data (Figure 4d) clarify this discrepancy where low $\delta$v values at altitudes below 3 km a.s.l. revealed a distinct aerosol layer near the surface for both events on 19 August~~, coinciding with the surface events and indicating~~ . The consequence of this pronounced aerosol layering above the station is that surface observations detected the arrival of smoke-dominated air masses~~at ground level. However, this layer was not detected in the~~ , whereas column-integrated ~~measurements due to~~ observations indicated the dominance of coarser desert dust particles~~in the upper atmosphere~~.

This local wildfire also had a direct impact on in situ atmospheric concentrations of $CO_2$, $CH_4$, and CO at IZO, which showed higher-than-usual values between 17 and 19 August (Figure 6). During the event, $CO_2$, $CH_4$, and CO concentrations increased significantly and reached peaks of approximately 520 ppm, 2800 ppb, and 12000 ppb, respectively, well above typical values at IZO (410-430 ppm for $CO_2$, 1800-2100 ppb for $CH_4$ and 50-200 ppb for CO). These marked increases (about 25 % for $CO_2$,

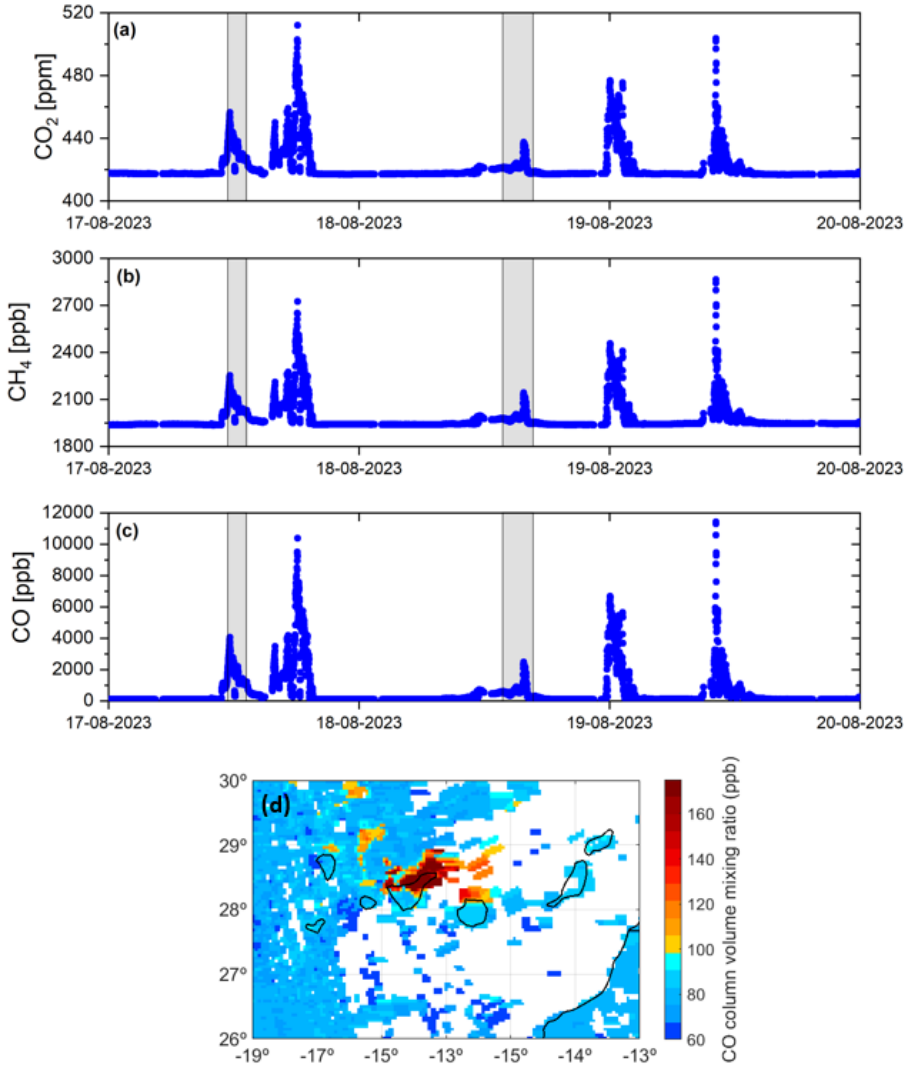


**Figure 6.** Time series of 1-minute averaged dry-air mole fractions of (a) $CO_2$ (ppm), (b) $CH_4$ (ppb) and (c) CO (ppb) from in situ measurements by the Picarro analyser at the Izaña Observatory between 17 and 19 August 2023. (d) Satellite CO total column from Copernicus Sentinel-5p TROPOMI over the Canary Islands between 17 and 19 August 2023 (using a 3-day moving average).

35 % for $CH_4$ and nearly two orders of magnitude for CO) are fully consistent with the presence of intense biomass-burning plumes over the observatory during the event, as confirmed by collateral smoke transport identified in Sentinel-5P TROPOMI CO observations (Figure 6d).

The temporal evolution of the in situ measurements reveals a strong correspondence between peaks in particulate matter ($PM_{10}$, $PM_{2.5}$), eBC, and greenhouse gases ($CO_2$, $CH_4$, CO) (Figure 5 and 6). All maxima occurred concurrently with the periods of highest columnar AOD and strongest backscatter in the lidar profiles. This simultaneity provides robust evidence that the observed perturbations in aerosol and gas concentrations originated from the same wildfire plume. These independent datasets confirm the coherent atmospheric signature of fresh biomass-burning emissions, reinforcing the interpretation of a strongly localised and intense smoke influence at Izaña during the 17–19 August events.

#### 4.1.1 ~~Spectral aerosol radiative forcing and efficiency~~

### 4.2 Spectral aerosol radiative forcing and efficiency

The influence of aerosols on spectral irradiance becomes evident when examining the spectra measured during the two days with the highest AOD (17 and 18 August 2023; Figure 4a). Figure 7 illustrates the pronounced variability observed in the $GHI_\lambda$, $DNI_\lambda$, and $DHI_\lambda$ components, highlighting the impact of these high-turbidity episodes, which lead to substantial spectral attenuation and angular redistribution of solar radiation. During the most intense smoke events, daily $GHI_\lambda$ was reduced by 21–27 %, $DNI_\lambda$ by 72–99 %, while $DHI_\lambda$ irradiance increased by 72–75 % compared with clean-sky conditions at IZO. These results are similar to those observed during the 2021 Greece wildfires, with decreases of 10–20 % in daily $GHI_\lambda$ (Masoom et al., 2023).

These measurements represent one of the few detailed spectral characterisations (300–1100 nm) of extreme biomass-burning aerosol episodes at a high-altitude observatory. The exceptionally large AOD values observed at IZO (up to 3.6 at 500 nm) place this event among the most intense smoke episodes documented.

The spectral radiative effects of biomass-burning aerosols were analysed at the times when the AOD at 500 nm (Figure 4 a, c, Table 1) reached its maximum values on each study day: 11:56 UTC (SZA 22.7°, AOD 3.63) on 17 August and 15:46 UTC (SZA 39.1°, AOD 2.25) on 18 August. Figure 8 shows the spectral distribution of irradiance, radiative forcing ($\Delta$F; W $m^{-2}nm^{-1}$), spectral AOD determined from EKO RSB measurements and radiative forcing efficiency ($\Delta F^{eff}$; W $m^{-2}nm^{-1}AOD^{-1}$). These large AOD values confirm the strong presence of smoke particles over the site, which substantially altered the radiative fluxes and their spectral distribution. Clear differences between the two days, as well as among the various SZA conditions, highlight the temporal evolution of the aerosol optical properties and their influence on surface radiation. The $\Delta F^{eff}$ was calculated using Equation 6, based on the spectral AOD retrieved at the EKO RSB wavelengths.

The differences between the two days reflect both the varying aerosol load and the changes in solar geometry, with the higher AOD and smaller SZA on 17 August enhancing the radiative impact. Slight variations in aerosol optical properties, including potential differences in fine-mode dominance or absorption, may also contribute to the observed contrast.

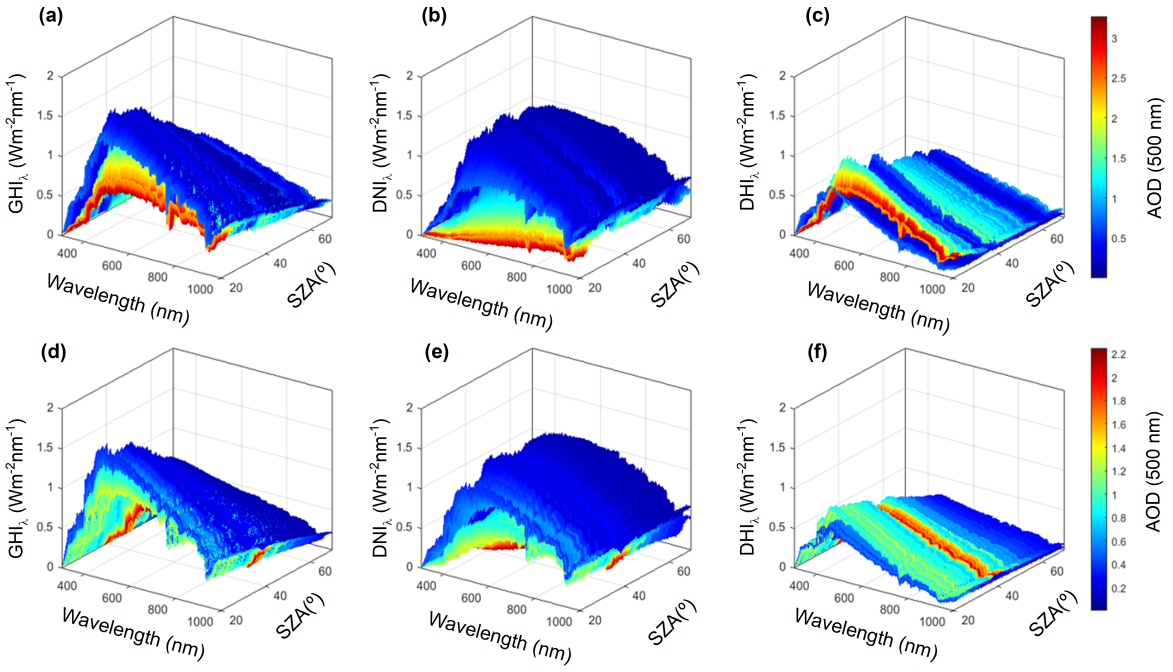


**Figure 7.** Spectral global-horizontal ($GHI_\lambda$), direct-normal ($DNI_\lambda$), and diffuse-horizontal ($DHI_\lambda$) irradiance measured on 17 August (a, b, c) and 18 August (d, e, f) 2023 between 06:30 and 19:50 UTC (a total of 793 spectra) using the EKO RSB at IZO. The colour bar shows the AOD at 500 nm retrieved from the EKO RSB measurements.

The spectral irradiance of $GHI_\lambda$, $DNI_\lambda$, and $DHI_\lambda$ exhibits a clear contrast between the measurements obtained under clean conditions (dashed lines) and those affected by fire events (solid lines) (Figure 8a, e). On both days, the high AOD caused a strong attenuation of $DNI_\lambda$ irradiance, mainly below 700 nm, accompanied by an enhancement of the $DHI_\lambda$ component. The stronger impact between 450 and 460 nm, with $\Delta$F values of -1.69 and -1.59 W $m^{-2}nm^{-1}$, respectively, indicates the dominance of fine-mode smoke particles which scatter efficiently short wavelengths. A pronounced attenuation of the $DNI_\lambda$ spectral irradiance and enhancement of the $DHI_\lambda$ component are observed, reflecting the strong scattering capacity of biomass-burning aerosols. This enhanced scattering capacity is consistent with the high SSA values obtained from the surface measurements (Fig. 5 in Sect. 4.1). The resulting spectra of $\Delta$F are negative for the $DNI_\lambda$ and $GHI_\lambda$ components and positive for the diffuse one, indicating a net surface cooling effect dominated by scattering processes. The magnitude of the $\Delta$F is larger on 17 August ($AOD_{500nm}$ = 3.63) than on 18 August ($AOD_{500nm}$ = 2.25), consistent with the higher aerosol load and the smaller solar zenith angle. The $\Delta F^{eff}$ spectra (Figure 8d, h) exhibit similar shapes for both days, with maximum efficiency in the visible region (400–800 nm), suggesting that the optical properties of the aerosols, likely dominated by biomass-burning particles, remained relatively constant throughout the episode.

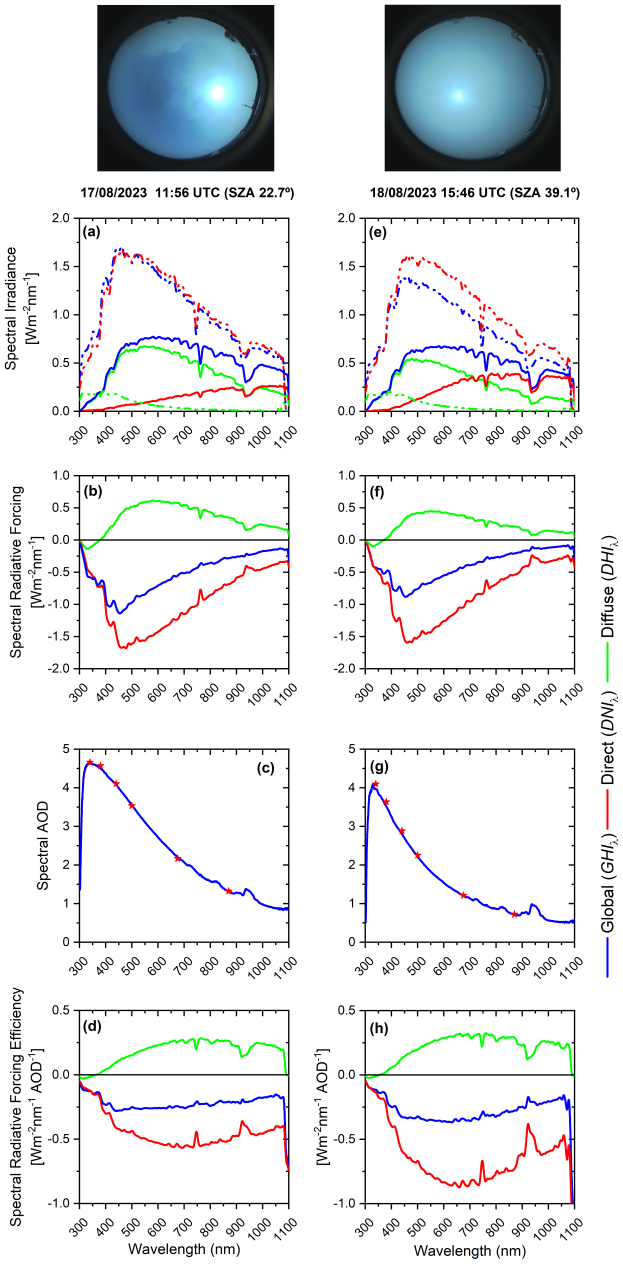


**Figure 8.** Spectral irradiance (W $m^{-2}nm^{-1}$) (a, e), spectral radiative forcing (W $m^{-2}nm^{-1}$) (b, f), spectral AOD obtained from EKO RSB measurements (blue line) and AOD obtained from CIMEL (red stars) (c,g), and spectral radiative forcing efficiency (W $m^{-2}nm^{-1}AOD^{-1}$) (d, h) for selected times corresponding to the two maximum AOD cases during the biomass-burning aerosol episode at IZO on 17 and 18 August 2023, with $AOD_{500nm}$ values of 3.63 and 2.25, respectively. The panels correspond to measurements at 11:56 UTC (SZA = 22.7°) on 17 August (a-d) and 15:46 UTC (SZA = 39.1°) on 18 August (e-h). The sky-camera images show the corresponding sky conditions at each time. Blue, red, and green lines represent global ($GHI_\lambda$) direct-normal ($DNI_\lambda$), and diffuse ($DHI_\lambda$) irradiance components, respectively. The dashed lines in panels (a, b) represent the spectra measured experimentally under clean conditions (6 August 2023 at 11:50 UTC, SZA = 22.6°, and 15:55 UTC, SZA = 39.1°).

The integrated spectral radiative forcing values ($\Delta$DF and $\Delta DF^{eff}$) determined from Equation 7 are shown in Table 2. The results are consistent with the spectral behaviour discussed in Figure 8. The total $\Delta DF^{GHI_\lambda}$ (300–1100 nm) reached -395 W m$^{-2}$ on 17 August and -299 W m$^{-2}$ on 18 August, confirming a strong surface cooling effect during the biomass-burning episode. The forcing was dominated by the $DNI_\lambda$ component ($\sim$ -700 and -609 W m$^{-2}$, respectively), while the $DHI_\lambda$ component partially compensated for this loss with positive values ($\sim$ +250 and +174 W m$^{-2}$), as expected under intense scattering conditions.

The band-integrated $\Delta F^{eff}$ exhibited a distinct spectral dependence, peaking in the visible range (-77 to -99 W m$^{-2}$AOD$^{-1}$ for the $GHI_\lambda$ component), consistent with the strong scattering capacity of fine-mode smoke particles. Near-IR efficiencies were slightly lower (-66 to -85 W m$^{-2}$AOD$^{-1}$), while UV contributions remained minor ($\sim$ -10 W m$^{-2}$AOD$^{-1}$). For the $DNI_\lambda$ component, $\Delta F^{eff}$ reached up to -211 W m$^{-2}$AOD$^{-1}$, whereas the $DHI_\lambda$ component showed positive values ($\sim$ +50–80 W m$^{-2}$AOD$^{-1}$), highlighting the enhanced scattering under high aerosol load. Integrated over 300–1100 nm, total $\Delta F^{eff}$ reached -154 W m$^{-2}$AOD$^{-1}$ on 17 August and -194 W m$^{-2}$AOD$^{-1}$ on 18 August, indicating a slightly higher radiative efficiency on the latter day despite lower AOD. These findings confirm that biomass-burning aerosols at IZO produced a marked shortwave surface cooling dominated by visible-range scattering processes.

Spectrally, for both $GHI_\lambda$ and $DNI_\lambda$ spectral radiation, the visible range (400–700 nm) contributed the most to the total forcing ($\sim$60–65 %), followed by the near-IR range ($\sim$22–25 % for $GHI_\lambda$ and $\sim$28–31 % for $DNI_\lambda$) and the UV range ($\sim$13 % for $GHI_\lambda$ and $\sim$7 % for $DNI_\lambda$) for the two days. This distribution matches the maximum in the incident solar irradiance and the high scattering efficiency of fine-mode smoke particles in the visible region. $\Delta F^{eff}$ also reflects the larger radiative impact per unit AOD on 18 August, despite the lower aerosol load, suggesting a slightly enhanced absorption or differences in aerosol optical properties and solar geometry. Overall, these integrated values confirm that biomass-burning aerosols at IZO produced a pronounced shortwave radiative cooling dominated by scattering processes, with maximum efficiency in the visible range.

Besides the instantaneous spectral and band-integrated values, daily radiative forcing was also computed to assess the accumulated shortwave impact of the smoke-laden days. On 17 August, the total daily forcing reached -56 ($GHI_\lambda$), -162 ($DNI_\lambda$), and +70 W m$^{-2}$ ($DHI_\lambda$), while on 18 August the corresponding values were -44, -137, and +60 W m$^{-2}$, respectively. The daily forcing efficiencies were -77, -313, and +138 W m$^{-2}$AOD$^{-1}$ for the $GHI_\lambda$, $DNI_\lambda$, and $DHI_\lambda$ components on 17 August, and -84, -332, and +145 W m$^{-2}$AOD$^{-1}$ on 18 August. These values are consistent with previously reported daily-scale radiative impacts of biomass-burning aerosols. For example, Zhuravleva et al. (2017) reported global radiative forcing values ranging from -13 to -60 W m$^{-2}$ and efficiencies between -80 and -40 W m$^{-2}$AOD$^{-1}$ during the 2012 Siberian wildfires.

In addition to the instantaneous spectral and band-integrated forcing values discussed above, the temporal evolution of the broadband shortwave radiative forcing was analysed over the two smoke-affected days in order to evaluate the diurnal behaviour of the aerosol perturbation (Figure 9). The time series shows a clear enhancement in the magnitude of the forcing during periods of strongest smoke influence, with the largest cooling occurring around local noon, when solar irradiance is at its maximum. On 17 August, the forcing exhibits a pronounced peak between approximately 11:30 and 13:30 UTC, coinciding with the period of highest aerosol loading observed at the station. On 18 August, the forcing remains significant over a broader time interval, with a maximum around 15:30 UTC, consistent with the later arrival of the densest smoke plume (Figure 4a).

**Table 2.** Averages of AOD (mean±std), ΔDF (W $m^{-2}$) and $\Delta DF^{eff}$ (W $m^{-2}$ $AOD^{-1}$) for $GHI_\lambda$, $DNI_\lambda$ and $DHI_\lambda$ spectral radiation components in the four spectral ranges (UV: 300–400 nm, VIS: 400–700 nm, near-IR: 700–1100 nm, and Total: 300-1100 nm) for the two study cases (17 August 11:56 UTC (SZA 22.7°) and 18 August 15:46 UTC (SZA 39.1°)).

| | AOD | $\Delta DF^{GHI_\lambda}$ ($\Delta DF^{eff-GHI_\lambda}$) $Wm^{-2}$ ($Wm^{-2}AOD^{-1}$) | $\Delta DF^{DNI_\lambda}$ ($\Delta DF^{eff-DNI_\lambda}$) $Wm^{-2}$ ($Wm^{-2}AOD^{-1}$) | $\Delta DF^{DHI_\lambda}$ ($\Delta DF^{eff-DHI_\lambda}$) $Wm^{-2}$ ($Wm^{-2}AOD^{-1}$) |
|---|---|---|---|---|
| **UV: 300–400 nm** | | | | |
| ~~17/08/2023~~ 17-08-2023 **11:56** | 4.75±0.06 | -52.8 (-11.1) | -51.8 (-10.9) | -5.0 (-1.0) |
| ~~18/08/2023~~ 18-08-2023 **15:46** | 3.98±0.33 | -39.0 (-10.1) | -47.1 (-12.4) | -2.5 (-0.5) |
| **VIS: 400–700 nm** | | | | |
| ~~17/08/2023~~ 17-08-2023 **11:56** | 3.21±0.76 | -246.0 (-76.6) | -429.5 (-139.0) | 150.3 (51.7) |
| ~~18/08/2023~~ 18-08-2023 **15:46** | 1.98±0.65 | -191.1 (-99.2) | -391.4 (-211.3) | 112.7 (64.9) |
| **near-IR: 700–1100 nm** | | | | |
| ~~17/08/2023~~ 17-08-2023 **11:56** | 1.42±0.31 | -95.4 (-65.7) | -217.7 (-149.8) | 105.5 (72.5) |
| ~~18/08/2023~~ 18-08-2023 **15:46** | 0.78±0.16 | -68.1 (-84.5) | -169.1 (-210.3) | 63.4 (79.0) |
| **Total: 300–1100 nm** | | | | |
| ~~17/08/2023~~ 17-08-2023 **11:56** | 2.64±1.30 | -394.9 (-153.7) | -699.9 (-300.0) | 251.1 (123.2) |
| ~~18/08/2023~~ 18-08-2023 **15:46** | 1.73±1.15 | -298.6 (-194.0) | -608.4 (-434.5) | 173.8 (143.5) |

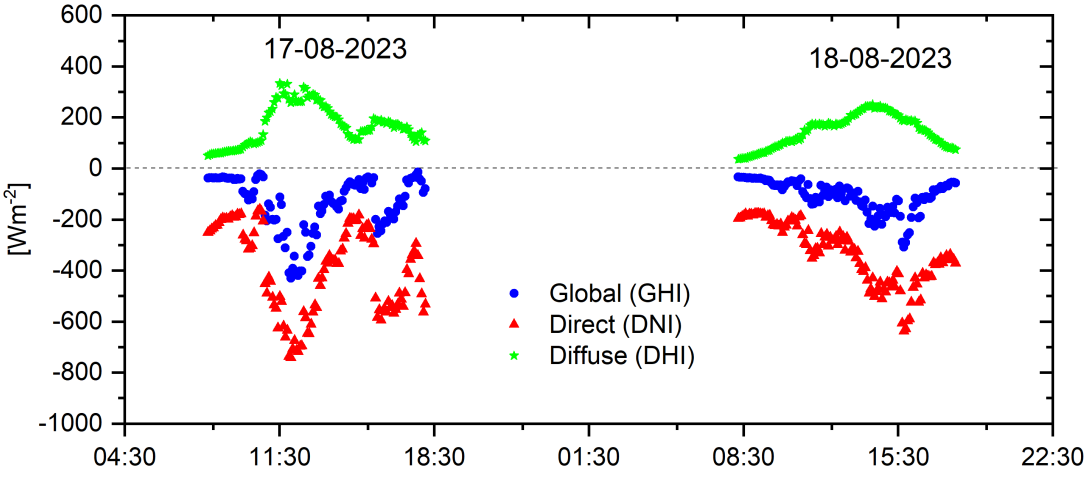


**Figure 9.** Temporal evolution of the radiative forcing components (blue: global (*GHI*), red: direct (*DNI*) and green: diffuse (*DHI*) radiation) at Izaña Observatory during the wildfire smoke events of 17 and 18 August 2023.

Although the magnitude observed at IZO lies among the highest documented due to the exceptional aerosol load, this comparison reinforces that the radiative response observed at IZO is consistent with the upper bounds of biomass-burning forcing reported in the literature.

## 5 Conclusions

The extreme wildfire episode affecting Tenerife in August 2023 resulted in an exceptional aerosol perturbation over the Izaña Observatory, characterised by an extraordinarily high aerosol load dominated by fine-mode smoke particles. The event reached $AOD_{500nm}$ (AE) values of 3.63 (1.71) and 2.25 (2.04) on 17 and 18 August 2023, respectively, among the highest ever reported at this high-mountain site, and was accompanied by fine-mode fractions exceeding 0.9, indicating the presence of freshly emitted biomass-burning aerosols. Spectral measurements revealed a strong attenuation of global ($GHI_\lambda$) and direct-normal ($DNI_\lambda$) irradiance, particularly at wavelengths below 700 nm where fine-mode scattering is most effective, along with a marked enhancement of diffuse irradiance ($DHI_\lambda$). As a result, daily global irradiance decreased by 21–27 %, while direct-normal irradiance nearly collapsed (-72 to -99 %), demonstrating the episode's strong radiative impact.

The radiative forcing analysis showed that scattering by fine-mode smoke dominated the shortwave response, with spectral forcing strongly negative for direct and global irradiance but positive for the diffuse component. Maximum forcing occurred in the visible region, consistent with the optical properties of freshly emitted smoke. On 17 and 18 August, shortwave integrated radiative forcing reached -395 and -299 W $m^{-2}$, respectively, confirming a strong surface cooling effect during the biomass-burning episode. On 17 August, total daily forcing amounted to -56 W $m^{-2}$ ($GHI_\lambda$), -162 W $m^{-2}$ ($DNI_\lambda$), and +70 W $m^{-2}$ (DHI$\lambda$), while on 18 August the corresponding values were -44, -137, and +60 W $m^{-2}$, respectively. The daily forcing efficiencies were -77, -313, and +138 W $m^{-2}AOD^{-1}$ for the $GHI_\lambda$, $DNI_\lambda$, and $DHI_\lambda$ components on 17 August, and -84, -332, and +145 W $m^{-2}AOD^{-1}$ on 18 August. These values are consistent with those reported by Zhuravleva et al. (2017) during the 2012 Siberian wildfires.

Complementary multi-platform observations reinforce this interpretation. Coincident increases in $PM_{10}$, $PM_{2.5}$, eBC, and combustion-related greenhouse gases ($CO_2$, $CH_4$, CO) demonstrate the direct influence of the wildfire plume on the atmospheric composition at IZO, providing a comprehensive picture of the physical and chemical signatures associated with an intense near-source smoke intrusion.

From a climate perspective, the magnitude and spectral signature of the radiative perturbations documented here highlight the importance of improving the representation of fine-mode smoke aerosols in radiative transfer models and Earth-system simulations. Current models can face difficulties in reproducing the optical complexity and high scattering efficiency of fresh biomass-burning aerosols, particularly when they are transported into the free troposphere through fire-induced vertical motion. As the frequency, intensity, and injection height of wildfire emissions are expected to evolve under future climate conditions, incorporating observationally informed parametrisations will help refine estimates of surface energy budgets, cloud–aerosol interactions, and regional climate responses. The extreme Tenerife episode therefore provides a useful reference case for

model evaluation and illustrates the value of coordinated observations for improving our understanding of wildfire–climate interactions.

*Data availability.* The EKO RSB data used in this study are available on request from the Izaña WMO-MLC. The AERONET data are freely available from the NASA Goddard Space Flight Center (https://aeronet.gsfc.nasa.gov; last access 4 December 2025). Data from MPLNET used in the present study can be obtained from https://mplnet.gsfc.nasa.gov/ (last access: 21 October, 2025). In situ surface data from the Izaña Atmospheric Observatory contribute to the WMO GAW program and are available from the World Data Centre for Greenhouse Gases (WDCGG, https://gaw.kishou.go.jp/policy/gaw/, last access: 26 October 2025). TROPOMI data (Copernicus Sentinel-5P) are publicly available from the Sentinel-5P data hub at https://maps.s5p-pal.com/co/ (last access: 3 December 2025). TSI nephelometer scattering coefficients and $PM_{10}$ MAAP equivalent black carbon data are publicly available through the EBAS database (https://ebas.nilu.no), the World Data Centre for Aerosols (WDAC) hosted by NILU. TEOM mass concentration data, and $PM_1$ MAAP equivalent black carbon data are available upon request to the authors.

*Author contributions.* All co-authors contributed to the preparation and writing of the manuscript. RDG, AB, and PGS designed the structure and methodology of the paper, discussed the results, and participated in the retrieval analysis. RDG wrote the main part of the paper and performed the required calculations. VC provided valuable ideas used in this study and guidance based on her experience in spectroradiometry and photometry. AB, PGS, YG, OA, and FA wrote Sections 2.3 and 4.1 related to remote sensing and in situ aerosol measurements. AAH, SLL, and PPR wrote Sections 2.3 and 4.1 related to greenhouse gases. JJB provided the meteorological data and its interpretation. RR performed the maintenance and daily checks of the EKO RSB spectroradiometer.

*Competing interests.* The contact author has declared that none of the authors has any competing interests.

*Acknowledgements.* This work is part of the activities of the WMO-Measurement Lead Centre for aerosols and water vapor remote sensing instruments (MLC). We gratefully acknowledge the data provided by the AERONET network (Izaña: Philippe Goloub, Emilio Cuevas and África Barreto). The AERONET sun photometers at the Izaña Observatory (IZO) were calibrated through the AEROSPAIN Central Facility (https://aerospain.aemet.es/, last access: 25 October 2025), supported by the European Community Research Infrastructure Action under the ACTRIS grant (agreement no. 871115). We gratefully acknowledge the data provided by the MPLNet network. The MPLNet project is funded by the NASA Radiation Sciences Program and the Earth Observing System. This study was carried out within the Global Atmospheric Watch (GAW) Programme at the Izaña Atmospheric Research Centre, operated by AEMET. We acknowledge the station staff and the GAW World Data Centre for maintaining and distributing the dataset. The authors would like to thank the libRadtran radiative transfer model team, whose tool was used to estimate the spectral irradiance under clean-sky conditions. The authors acknowledge the support from the IZO staff for maintaining the instrumentation. This work was supported by the Ministerio de Ciencia e Innovación (MICINN), grants no. PID2021-127588OB-I00 and PID2024-157697OB-I00. This work was also funded by the European Comision through the EUBURN-RISK project

(INTERREG-SUDOE; S2/2.4/F0327). The authors acknowledge the support of COST Action HARMONIA (CA21119) and the Spanish Ministry for Science and Innovation to ACTRIS-ERIC.

## References


AEMET: Candelaria — Depósito Cuevecitas en Agosto de 2023. Observación Meteorológica Horaria, https://x-y.es/aemet/est-C438N-candelaria-deposito-cuevecitas?mes=2023-08, last access: 29 Novembrer 2025, 2023.

AEMET: Olas de Calor en España Desde 1975 (Diciembre de 2024), https://www.aemet.es/documentos/es/conocermas/recursos_en_linea/publicaciones_y_estudios/estudios/Olas_calor/olas_calor_actualizacion_dic24.pdf, last access: 29 Novembrer 2025, 2024.

Amatulli, G., Camia, A., and San-Miguel-Ayanz, J.: Estimating future burned areas under changing climate in the EU-Mediterranean countries, Science of The Total Environment, 450-451, 209–222, https://doi.org/10.1016/j.scitotenv.2013.02.014, 2013.

Anderson, T. L. and Ogren, J. A.: Determining Aerosol Radiative Properties Using the TSI 3563 Integrating Nephelometer, Aerosol Science and Technology, 29, 57–69, https://doi.org/10.1080/02786829808965551, 1998.

Ångström, A.: On the atmospheric transmission of sun radiation. II, Geografiska Annaler, 12, 130–159, 1930.

Barreto, A., Cuevas, E., Granados-Muñoz, M.-J., Alados-Arboledas, L., Romero, P. M., Gröbner, J., Kouremeti, N., Almansa, A. F., Stone, T., Toledano, C., Román, R., Sorokin, M., Holben, B., Canini, M., and Yela, M.: The new sun-sky-lunar Cimel CE318-T multiband photometer – a comprehensive performance evaluation, Atmospheric Measurement Techniques, 9, 631–654, https://doi.org/10.5194/amt-9-631-2016, 2016.

Barreto, A., Cuevas, E., García, R. D., Carrillo, J., Prospero, J. M., Ilić, L., Basart, S., Berjón, A. J., Marrero, C. L., Hernández, Y., Bustos, J. J., Ničković, S., and Yela, M.: Long-term characterisation of the vertical structure of the Saharan Air Layer over the Canary Islands using lidar and radiosonde profiles: implications for radiative and cloud processes over the subtropical Atlantic Ocean, Atmospheric Chemistry and Physics, 22, 739–763, https://doi.org/10.5194/acp-22-739-2022, 2022.

Cachorro, V. E., García, V. M., and Garcia, R. D.: Spectral Solar Irradiance Estimation Under Clear Sky, in: Spectral Characteristics of Solar Radiation: Applications in Photovoltaic Conversion, edited by Badescu, V. and Paulescu, M., chap. 5, Elsevier, 1 edn., ISBN 9780443238383, eBook ISBN, 2025.

Campbell, J. R., Hlavka, D. L., Welton, E. J., Flynn, C. J., Turner, D. D., Spinhirne, J. D., Scott, V. S., and Hwang, I. H.: Full-Time, Eye-Safe Cloud and Aerosol Lidar Observation at Atmospheric Radiation Measurement Program Sites: Instruments and Data Processing, J. Atmos. Ocean. Tech., 19, 431–442, https://doi.org/10.1175/1520-0426(2002)019<0431:FTESCA>2.0.CO;2, 2002.

Correa, J. and Dorta, P.: Assessment of Large Forest Fires in the Canary Islands and Their Relationship with Subsidence Thermal Inversion and Atmospheric Conditions, Geographies, 5, https://doi.org/10.3390/geographies5030037, 2025.

Correa, J., Boulat, L., and Dorta, P.: Forest Fires, Vulnerability, and Exposure: The Evaluation of What Was Salvaged in the 2023 Fire in Tenerife (Spain), Fire, 8, https://doi.org/10.3390/fire8050186, 2025.

Crosson, E.: A cavity ring-down analyzer for measuring atmospheric levels of methane, carbon dioxide, and water vapor, Applied Physics B: Lasers and Optics, 92, 403–408, https://doi.org/10.1007/s00340-008-3135-y, 2008.

Cuevas, E., González, Y., Rodríguez, S., Guerra, J. C., Gómez-Peláez, A. J., Alonso-Pérez, S., Bustos, J., and Milford, C.: Assessment of atmospheric processes driving ozone variations in the subtropical North Atlantic free troposphere, Atmos. Chem. Phys., 13, 1973–1998, https://doi.org/10.5194/acp-13-1973-2013, 2013.

Cuevas, E., Gómez-Peláez, A., Rodríguez, S., Terradellas, E., Basart, S., García, R., García, O., and Alonso-Pérez, S.: The pulsating nature of large-scale Saharan dust transport as a result of interplays between mid-latitude Rossby waves and the North African Dipole Intensity, Atmospheric Environment, 167, 586–602, https://doi.org/10.1016/j.atmosenv.2017.08.059, 2017.

Cuevas, E., Milford, C., Barreto, A., Bustos, J. J., García, R. D., Marrero, C. L., Prats, N., Bayo, C., Ramos, R., Terradellas, E., Suárez, D., Rodríguez, S., de la Rosa, J., Vilches, J., Basart, S., Werner, E., López-Villarrubia, E., Rodríguez-Mireles, S., Pita Toledo, M. L., González, O., Belmonte, J., Puigdemunt, R., Lorenzo, J. A., Oromí, P., and del Campo-Hernández, R.: Desert Dust Outbreak in the Canary Islands (February 2020): Assessment and Impacts, Tech. rep., State Meteorological Agency (AEMET) and World Meteorological Organization (WMO), Madrid, Spain and Geneva, Switzerland, https://library.wmo.int/idurl/4/43183, 2021.

Cuevas, E., García, O. E., León-Luis, S. F., González-Dávila, M., Adame, J. A., Carrara, A., Vélez-Belchí, P., Delory, E., Rivas-Soriano, P. P., Villalba-Méndez, G., Barreto, A., Curcoll, R., Yela, M., and González-González, A.: ICOS-SPAIN Activity Report 2021–2022, State Meteorological Agency (AEMET), Madrid, Spain, https://doi.org/10.31978/666-23-010-3, nIPO: 666-23-010-3, 2023.

Cuevas, E., Milford, C., Barreto, A., Bustos, J. J., García, O. E., García, R. D., Marrero, C., Prats, N., Ramos, R., Redondas, A., Reyes, E., Rivas-Soriano, P. P., Romero-Campos, P. M., Torres, C. J., Schneider, M., Yela, M., Belmonte, J., Almansa, F., López-Solano, C., Basart, S., Werner, E., Rodríguez, S., Alcántara, A., Alvarez, O., Bayo, C., Berjón, A., Borges, A., Carreño, V., Castro, N. J., Chinea, N., Cruz, A. M., Damas, M., G. Y., Hernández, C., Hernández, J., León-Luís, S. F., López-Fernández, R., López-Solano, J., Mármol, I., Martín, T., Parra, F., Rodríguez-Valido, M., Santana, D., Santo-Tomás, F., and Serrano, A.: Izaña Atmospheric Research Center Activity Report 2021-2022., Tech. Rep. WMO/GAW No. 290, World Meteorological Organization & Izaña Atmospheric Resear Center (AEMET), available at: https://www.aemet.es/documentos/es/conocermas/recursos_en_linea/publicaciones_y_estudios/publicaciones/Izana_Report/Izana_Report_2021_2022.pdf, 2024.

Cunningham, C. X., Williamson, G. J., and Bowman, D. M. J. S.: Increasing frequency and intensity of the most extreme wildfires on Earth, Nature Ecology & Evolution, 8, 1420–1425, https://doi.org/10.1038/s41559-024-02452-2, 2024.

Dahlbäck, O. and Stammes, P.: A new spherical model for computing the radiation field available for photolysis and heating at twilight, Planetary and Space Science, 39, 671–683, https://doi.org/10.1016/0032-0633(91)90054-8, 1991.

Eck, T. F., Holben, B. N., Ward, D. E., Dubovik, O., Reid, J. S., Smirnov, A., Mukelabai, M. M., Hsu, N. C., O'Neill, N. T., and Slutsker, I.: Characterization of the optical properties of biomass burning aerosols in Zambia during the 1997 ZIBBEE field campaign, Journal of Geophysical Research: Atmospheres, 106, 3425–3448, https://doi.org/10.1029/2000JD900555, 2001.

Elmqvist, T., Valkó, O., Stoof, C., Aakala, T., Arca, B., Arianoutsou, M., Arsava, K., Ascoli, D., Bengtsson, J., Castro, R., Engelbrecht, J., Fra Paleo, U., Granström, A., Ibisch, P., Kalabokidis, K., Kandárová, H., Marinšek, A., Knottnerus, A., Metallinou, M., Müller, M., Oliveira, T., Pereira, J. M. C., Plieninger, T., Palaiologou, P., Pulido Diaz, F., Saražin, J., Stoyanov, T., Newman Thacker, F., van der Werf, G., and Zerefos, C.: Changing Wildfires: Policy Options for a Fire-literate and Fire-adapted Europe, Easac policy report 48, European Academies' Science Advisory Council (EASAC), ISBN 978-3-7001-9739-3, https://www.easac.eu, 2025.

Emde, C., Buras-Schnell, R., Kylling, A., Mayer, B., Gasteiger, J., Hamann, U., Kylling, J., Richter, B., Pause, C., Dowling, T., et al.: The libRadtran software package for radiative transfer calculations (version 2.0. 1), Geoscientific Model Development, pp. 1647–1672, https://doi.org/10.5194/gmd-9-1647-2016, 2016.

Filonchyk, M. and Peterson, M. P.: Changes in aerosol properties at the El Arenosillo site in Southern Europe as a result of the 2023 Canadian forest fires, Environmental Research, 260, 119 629, https://doi.org/10.1016/j.envres.2024.119629, 2024.

Flynn, C. J., Mendoza, A., Zheng, Y., and Mathur, S.: Novel polarization-sensitive micropulse lidar measurement technique, Opt. Express, 15, 2785–2790, https://doi.org/10.1364/OE.15.002785, 2007.

Forster, P., Storelvmo, T., Armour, K., Collins, W., Dufresne, J.-L., Frame, D., Lunt, D. J., Mauritsen, T., Palmer, M. D., Watanabe, M., Wild, M., and Zhang, H.: The Earth's Energy Budget, Climate Feedbacks, and Climate Sensitivity, in: Climate Change 2021: The Physical Science Basis. Contribution of Working Group I to the Sixth Assessment Report of the Intergovernmental Panel on Climate Change,

edited by Masson-Delmotte, V., Zhai, P., Pirani, A., Connors, S. L., Péan, C., Berger, S., Caud, N., Chen, Y., Goldfarb, L., Gomis, M. I., Huang, M., Leitzell, K., Lonnoy, E., Matthews, J. B. R., Maycock, T. K., Waterfield, T., Yelekçi, O., Yu, R., and Zhou, B., pp. 923–1054, Cambridge University Press, Cambridge, United Kingdom and New York, NY, USA, https://doi.org/10.1017/9781009157896.009, 2021.

García, R. D., Cuevas, E., Ramos, R., Cachorro, V. E., Redondas, A., and Moreno-Ruiz, J. A.: Description of the Baseline Surface Radiation Network (BSRN) station at the Izaña Observatory (2009–2017): measurements and quality control/assurance procedures, Geoscientific Instrumentation, Methods and Data Systems, 8, 77–96, https://doi.org/10.5194/gi-8-77-2019, 2019.

García, R. D., García, O. E., Cuevas, E., Cachorro, V. E., Romero-Campos, P. M., Ramos, R., and de Frutos, A. M.: Solar radiation measurements compared to simulations at the BSRN Izaña station. Mineral dust radiative forcing and efficiency study, Journal of Geophysical Research: Atmospheres, 119, 179–194, https://doi.org/10.1002/2013JD020301, 2014.

García, R. D., Cuevas, E., Barreto, , Cachorro, V. E., Pó, M., Ramos, R., and Hoogendijk, K.: Aerosol retrievals from the EKO MS-711 spectral direct irradiance measurements and corrections of the circumsolar radiation, Atmospheric Measurement Techniques, 13, 2601–2621, https://doi.org/10.5194/amt-13-2601-2020, 2020.

García, R. D., García, O. E., Cuevas-Agulló, E., Barreto, , Cachorro, V. E., Marrero, C., Almansa, F., Ramos, R., and Pó, M.: Spectral Aerosol Radiative Forcing and Efficiency of the La Palma Volcanic Plume over the Izaña Observatory, Remote Sensing, 15, https://doi.org/10.3390/rs15010173, 2023.

Giles, D. M., Sinyuk, A., Sorokin, M. G., Schafer, J. S., Smirnov, A., Slutsker, I., Eck, T. F., Holben, B. N., Lewis, J. R., Campbell, J. R., Welton, E. J., Korkin, S. V., and Lyapustin, A. I.: Advancements in the Aerosol Robotic Network (AERONET) Version 3 database – automated near-real-time quality control algorithm with improved cloud screening for Sun photometer aerosol optical depth (AOD) measurements, Atmospheric Measurement Techniques, 12, 169–209, https://doi.org/10.5194/amt-12-169-2019, 2019.

González, Y., Sánchez-Barrero, M. F., Popovici, I., Barreto, A., Victori, S., Welton, E. J., García, R. D., Sicilia, P. G., Almansa, F. A., Torres, C., and Goloub, P.: Compact dual-wavelength depolarization lidar for aerosol characterization over the subtropical North Atlantic, Atmospheric Measurement Techniques, 18, 1885–1908, https://doi.org/10.5194/amt-18-1885-2025, 2025.

Guo, Z., Li, W., Ciais, P., Sitch, S., van der Werf, G. R., Bowring, S. P. K., Bastos, A., Mouillot, F., He, J., Sun, M., Zhu, L., Du, X., Wang, N., and Huang, X.: Reconstructed global monthly burned area maps from 1901 to 2020, Earth System Science Data, 17, 3599–3618, https://doi.org/10.5194/essd-17-3599-2025, 2025.

Gómez-Pelaez, A. J., Ramos, R., Cuevas, E., Gómez-Trueba, V., and Reyes, E.: Atmospheric $CO_2$, $CH_4$, and CO with the CRDS technique at the Izaña Global GAW station: instrumental tests, developments, and first measurement results, Atmospheric Measurement Techniques, 12, 2043–2066, https://doi.org/10.5194/amt-12-2043-2019, 2019.

Haarig, M., Ansmann, A., Baars, H., Jimenez, C., Veselovskii, I., Engelmann, R., and Althausen, D.: Depolarization and lidar ratios at 355, 532, and 1064 nm and microphysical properties of aged tropospheric and stratospheric Canadian wildfire smoke, Atmospheric Chemistry and Physics, 18, 11 847–11 861, https://doi.org/10.5194/acp-18-11847-2018, 2018.

Heintzenberg, J., Wiedensohler, A., Tuch, T., Covert, D., Sheridan, P., Ogren, J., Gras, J., Nessler, R., Kleefeld, C., Kalivitis, N., et al.: Intercomparisons and aerosol calibrations of 12 commercial integrating nephelometers of three manufacturers, Journal of Atmospheric and Oceanic Technology, 23, 902–914, 2006.

Holben, B., Eck, T., Slutsker, I., Tanré, D., Buis, J., Setzer, A., Vermote, E., Reagan, J., Kaufman, Y., Nakajima, T., Lavenu, F., Jankowiak, I., and Smirnov, A.: AERONET—A Federated Instrument Network and Data Archive for Aerosol Characterization, Remote Sensing of Environment, 66, 1 – 16, https://doi.org/10.1016/S0034-4257(98)00031-5, 1998.

IPCC: Climate Change 2013: The Physical Science Basis. Contribution of Working Group I to the Fifth Assessment Report of the Intergovernmental Panel on Climate Change, Cambridge University Press, Cambridge, United Kingdom and New York, NY, USA, https://doi.org/10.1017/CBO9781107415324, fifth Assessment Report (AR5), 2013.

IPCC: Climate Change 2023: Synthesis Report. Contribution of Working Groups I, II and III to the Sixth Assessment Report of the Intergovernmental Panel on Climate Change, Intergovernmental Panel on Climate Change, Geneva, Switzerland, https://doi.org/10.59327/IPCC/AR6-9789291691647, edited by Core Writing Team; Lee, H. and Romero, J. (eds.), 2023.

Jones, M. W., Kelley, D. I., Burton, C. A., Di Giuseppe, F., Barbosa, M. L. F., Brambleby, E., Hartley, A. J., Lombardi, A., Mataveli, G., McNorton, J. R., Spuler, F. R., Wessel, J. B., Abatzoglou, J. T., Anderson, L. O., Andela, N., Archibald, S., Armenteras, D., Burke, E., Carmenta, R., Chuvieco, E., Clarke, H., Doerr, S. H., Fernandes, P. M., Giglio, L., Hamilton, D. S., Hantson, S., Harris, S., Jain, P., Kolden, C. A., Kurvits, T., Lampe, S., Meier, S., New, S., Parrington, M., Perron, M. M. G., Qu, Y., Ribeiro, N. S., Saharjo, B. H., San-Miguel-Ayanz, J., Shuman, J. K., Tanpipat, V., van der Werf, G. R., Veraverbeke, S., and Xanthopoulos, G.: State of Wildfires 2023–2024, Earth System Science Data, 16, 3601–3685, https://doi.org/10.5194/essd-16-3601-2024, 2024.

Koukouli, M.-E., Pseftogkas, A., Karagkiozidis, D., Mermigkas, M., Panou, T., Balis, D., and Bais, A.: Extreme wildfires over Northern Greece during Summer 2023 – Part B. Adverse effects on regional air quality, Atmospheric Research, 320, 108 034, https://doi.org/10.1016/j.atmosres.2025.108034, 2025.

Laj, P. et al.: Aerosol, Clouds and Trace Gases Research Infrastructure (ACTRIS): The European Research Infrastructure Supporting Atmospheric Science, Bulletin of the American Meteorological Society, 105, E1397–E1426, https://doi.org/10.1175/BAMS-D-23-0064.1, 2024.

Long, C. N. and Ackerman, T. P.: Identification of clear skies from broadband pyranometer measurements and calculation of downwelling shortwave cloud effects, Journal of Geophysical Research: Atmospheres, 105, 15 609–15 626, https://doi.org/10.1029/2000JD900077, 2000.

Masoom, A., Fountoulakis, I., Kazadzis, S., Raptis, I.-P., Kampouri, A., Psiloglou, B. E., Kouklaki, D., Papachristopoulou, K., Marinou, E., Solomos, S., Gialitaki, A., Founda, D., Salamalikis, V., Kaskaoutis, D., Kouremeti, N., Mihalopoulos, N., Amiridis, V., Kazantzidis, A., Papayannis, A., Zerefos, C. S., and Eleftheratos, K.: Investigation of the effects of the Greek extreme wildfires of August 2021 on air quality and spectral solar irradiance, Atmospheric Chemistry and Physics, 23, 8487–8514, https://doi.org/10.5194/acp-23-8487-2023, 2023.

Mayer, B. and Kylling, A.: Technical note: The libRadtran software package for radiative transfer calculations - description and examples of use, Atmospheric Chemistry and Physics, 5, 1855–1877, https://doi.org/10.5194/acp-5-1855-2005, 2005.

Michailidis, K., Garane, K., Karagkiozidis, D., Peletidou, G., Voudouri, K.-A., Balis, D., and Bais, A.: Extreme wildfires over northern Greece during summer 2023 – Part A: Effects on aerosol optical properties and solar UV radiation, Atmospheric Research, 311, 107 700, https://doi.org/10.1016/j.atmosres.2024.107700, 2024.

Müller, T., Henzing, J. S., de Leeuw, G., Wiedensohler, A., Alastuey, A., Angelov, H., Bizjak, M., Collaud Coen, M., Engström, J. E., Gruening, C., Hillamo, R., Hoffer, A., Imre, K., Ivanow, P., Jennings, G., Sun, J. Y., Kalivitis, N., Karlsson, H., Komppula, M., Laj, P., Li, S.-M., Lunder, C., Marinoni, A., Martins dos Santos, S., Moerman, M., Nowak, A., Ogren, J. A., Petzold, A., Pichon, J. M., Rodriquez, S., Sharma, S., Sheridan, P. J., Teinilä, K., Tuch, T., Viana, M., Virkkula, A., Weingartner, E., Wilhelm, R., and Wang, Y. Q.: Characterization and intercomparison of aerosol absorption photometers: result of two intercomparison workshops, Atmospheric Measurement Techniques, 4, 245–268, https://doi.org/10.5194/amt-4-245-2011, 2011.

Navarro, G., Caballero, I., Silva, G., Parra, P.-C., Águeda Vázquez, and Caldeira, R.: Evaluation of forest fire on Madeira Island using Sentinel-2A MSI imagery, International Journal of Applied Earth Observation and Geoinformation, 58, 97–106, https://doi.org/10.1016/j.jag.2017.02.003, 2017.

Nepomuceno Pereira, S., Preißler, J., Guerrero-Rascado, J. L., Silva, A. M., and Wagner, F.: Forest Fire Smoke Layers Observed in the Free Troposphere over Portugal with a Multiwavelength Raman Lidar: Optical and Microphysical Properties, The Scientific World Journal, 2014, 421 838, https://doi.org/10.1155/2014/421838, 2014.

O'Neill, N. T., Eck, T. F., Smirnov, A., Holben, B. N., and Thulasiraman, S.: Spectral discrimination of coarse and fine mode optical depth, Journal of Geophysical Research: Atmospheres, 108, https://doi.org/10.1029/2002JD002975, 2003.

O'Neill, N. T., Ranjbar, K., Ivănescu, L., Eck, T. F., Reid, J. S., Giles, D. M., Pérez-Ramírez, D., and Chaubey, J. P.: Relationship between the sub-micron fraction (SMF) and fine-mode fraction (FMF) in the context of AERONET retrievals, Atmospheric Measurement Techniques, 16, 1103–1120, https://doi.org/10.5194/amt-16-1103-2023, 2023.

Patashnick, H., Rupprecht, G., of Mines, U. S. B., Co, R. . P., of Mines. Mining Research, U. S. B., for Occupational Safety, N. I., and Health: Personal Dust Exposure Monitor Based on the Tapered Element Oscillating Microbalance, Mining research contract report, Bureau of Mines, U.S. Department of the Interior, https://books.google.es/books?id=9psPGwAACAAJ, 1983.

Petzold, A. and Schönlinner, M.: Multi-angle absorption photometry—a new method for the measurement of aerosol light absorption and atmospheric black carbon, Journal of Aerosol Science, 35, 421–441, https://doi.org/10.1016/j.jaerosci.2003.09.005, 2004.

Petzold, A., Ogren, J. A., Fiebig, M., Laj, P., Li, S.-M., Baltensperger, U., Holzer-Popp, T., Kinne, S., Pappalardo, G., Sugimoto, N., Wehrli, C., Wiedensohler, A., and Zhang, X.-Y.: Recommendations for reporting "black carbon" measurements, Atmospheric Chemistry and Physics, 13, 8365–8379, https://doi.org/10.5194/acp-13-8365-2013, 2013.

Pó, M., Hoogendijk, K., Beuttell, W., Kazunori, S., and Takeuchi, E.: Direct spectral irradiance measurements from rotating Shadowband EKO grating spectroradiometer, in: 2018 IEEE 7th World Conference on Photovoltaic Energy Conversion (WCPEC)(A Joint Conference of 45th IEEE PVSC, 28th PVSEC & 34th EU PVSEC), pp. 2337–2340, IEEE, 2018.

Rodríguez, S., Alastuey, A., Alonso-Pérez, S., Querol, X., Cuevas, E., Abreu-Afonso, J., Viana, M., Pérez, N., Pandolfi, M., and de la Rosa, J.: Transport of desert dust mixed with North African industrial pollutants in the subtropical Saharan Air Layer, Atmospheric Chemistry and Physics, 11, 6663–6685, https://doi.org/10.5194/acp-11-6663-2011, 2011.

Rodríguez, S., Alastuey, A., and Querol, X.: A review of methods for long term in situ characterization of aerosol dust, Aeolian Research, 6, 55–74, https://doi.org/10.1016/j.aeolia.2012.07.004, 2012.

San-Miguel-Ayanz, J., Durrant, T., Boca, R., Maianti, P., Libertà, G., Oom, D. J. F., Branco, A., De Rigo, D., Suarez-Moreno, M., Ferrari, D., Roglia, E., Scionti, N., Broglia, M., Onida, M., Tistan, A., and Loffler, P.: Forest Fires in Europe, Middle East and North Africa 2022, Tech. rep., Publications Office of the European Union, Luxembourg, https://doi.org/10.2760/348120, 2023.

Sicard, M., Mallet, M., García-Vizcaíno, D., Comerón, A., Rocadenbosch, F., Dubuisson, P., and Muñoz-Porcar, C.: Intense dust and extremely fresh biomass burning outbreak in Barcelona, Spain: characterization of their optical properties and estimation of their direct radiative forcing, Environmental Research Letters, 7, 034 016, https://doi.org/10.1088/1748-9326/7/3/034016, 2012.

Stamnes, K., Tsay, S.-C., Wiscombe, W., and Jayaweera, K.: Numerically stable algorithm for discrete-ordinate-method radiative transfer in multiple scattering and emitting layered media, Applied optics, 27, 2502–2509, https://doi.org/10.1364/AO.27.002502, 1988.

Takamura, T. and Khatri, P.: Uncertainties in radiation measurement using a rotating shadow-band spectroradiometer, Journal of the Meteorological Society of Japan. Ser. II, 99, 1547–1561, https://doi.org/10.2151/jmsj.2021-075, 2021.

Toledano, C., González, R., Fuertes, D., Cuevas, E., Eck, T. F., Kazadzis, S., Kouremeti, N., Gröbner, J., Goloub, P., Blarel, L., Román, R., Barreto, A., Berjón, A., Holben, B. N., and Cachorro, V. E.: Assessment of Sun photometer Langley calibration at the high-elevation sites Mauna Loa and Izaña, Atmospheric Chemistry and Physics, 18, 14 555–14 567, https://doi.org/10.5194/acp-18-14555-2018, 2018.

Torres, B., Toledano, C., Berjón, A., Fuertes, D., Molina, V., Gonzalez, R., Canini, M., Cachorro, V. E., Goloub, P., Podvin, T., Blarel, L., Dubovik, O., Bennouna, Y., and de Frutos, A. M.: Measurements on pointing error and field of view of Cimel-318 Sun photometers in the scope of AERONET, Atmos. Meas. Tech., 6, 2207–2220, https://doi.org/10.5194/amt-6-2207-2013, 2013.

Valenzuela, A., Olmo, F., Lyamani, H., Antón, M., Titos, G., Cazorla, A., and Alados-Arboledas, L.: Aerosol scattering and absorption Ångström exponents as indicators of dust and dust-free days over Granada (Spain), Atmospheric Research, 154, 1–13, https://doi.org/10.1016/j.atmosres.2014.10.015, 2015.

Welton, E., Stewart, S., Lewis, J., Belcher, L., Campbell, J., and S., L.: Status of the NASA Micro Pulse Lidar Network (MPLNET): Overview of the network and future plans, new Version 3 data products, and the polarized MPL, EPJ Web of Conferences, 176, https://doi.org/10.1051/epjconf/201817609003, 2018.

Welton, E. J., Campbell, J. R., Spinhirne, J. D., and Scott, V. S.: Global monitoring of clouds and aerosols using a network of micropulse lidar systems, in: Lidar Remote Sens. for Industry and Environment Monitoring, vol. 4153, pp. 4153 – 4153 – 8, https://doi.org/10.1117/12.417040, 2001.

WMO: WMO Air Quality and Climate Bulletin No. 3 – September 2023, https://library.wmo.int/records/item/62090-no-3-september-2023?language_id=13&back=&offset=92, accessed: 2025-11-28, 2023.

Zhuravleva, T. B., Kabanov, D. M., Nasrtdinov, I. M., Russkova, T. V., Sakerin, S. M., Smirnov, A., and Holben, B. N.: Radiative characteristics of aerosol during extreme fire event over Siberia in summer 2012, Atmospheric Measurement Techniques, 10, 179–198, https://doi.org/10.5194/amt-10-179-2017, 2017.